J. Fluid Mech. (2002), *vol.* 458, *pp.* 303–332. © 2002 Cambridge University Press
DOI: 10.1017/S0022112002007887 Printed in the United Kingdom

The turbulent wake of two side-by-side circular cylinders

By Y. ZHOU, H. J. ZHANG AND M. W. YIU

Department of Mechanical Engineering, The Hong Kong Polytechnic University, Hung Hom, Kowloon, Hong Kong

mmyzhou@polyu.edu.hk

(Received 20 October 2000 and in revised form 25 October 2001)

This work is an experimental study of the turbulent vortex structures, and heat and momentum transport in the wake of two side-by-side circular cylinders. The spacing T between the cylinder axes was varied from $1.5d$ to $3d$ (d is the cylinder diameter). Both cylinders were slightly heated. A movable three-wire probe measured the velocity and temperature fluctuations, and an X-wire provided a phase reference. Measurements were conducted at $x/d = 10$, 20 and 40 at a Reynolds number of 5800 (based on d and the free-stream velocity U_∞). At $T/d = 1.5$, the phase-averaged velocity and temperature fields display a single vortex street. The two rows of vortices exhibit a significant difference in the maximum vorticity, size and lateral distance from the flow centreline. As T/d is increased to 3.0, the flow is totally different. Two antiphase streets occur initially. They are less stable, with vortices weakening faster, than the street at $T/d = 1.5$. By $x/d = 40$, one street only is identifiable. Effective vorticity flux density indicates that, while the outer vortex nearer to the free stream interacts largely with the adjacent oppositely signed inner vortices located near the flow centreline, the inner vortex interacts with the cross-stream inner vortices as well as with adjacent outer vortices. As a result, vorticity associated with the inner vortex is annihilated quicker than that associated with the outer vortex, leading to the early disappearance of inner vortices and formation of a single street. The contribution of the coherent motion of various Reynolds-averaged quantities such as the momentum and heat fluxes has also been quantified and discussed in conjunction with the vortex structures of the flow and temperature fields.

1. Introduction

The flow around two side-by-side cylinders is inherently important and of practical significance in many branches of engineering (Zdravkovich 1997; Sumner *et al.* 1999). The type of flow behind two side-by-side cylinders depends on the ratio T/d (T is the centre-to-centre cylinder spacing and d is the cylinder diameter) and other parameters, e.g. initial conditions, pressure gradient and Reynolds number (Re). At $T/d < 1.2$, the two cylinders behave like one structure, generating a single street (Sumner *et al.* 1999). For $1.5 < T/d < 2.0$, the gap flow between the cylinders is deflected, resulting in one wide and one narrow wake. The deflected gap flow is bi-stable and randomly changes over from one side to the other (Ishigai *et al.* 1972; Bearman & Wadcock 1973). The timescale for the changeover is several orders of magnitude longer than that of vortex shedding and of the instability of the separated shear flows (Kim & Durbin 1988). The deflected gap flow nature is nominally independent of Re. As T/d is

https://doi.org/10.1017/S0022112002007887 Published online by Cambridge University Press

increased beyond 2, two distinct vortex streets have been observed (Landweber 1942). The two streets are coupled, with a definite phase relationship. Williamson (1985) showed at $Re = 100$–200 ($Re \equiv U_\infty d/\nu$, where U_∞ is the free-stream velocity and ν is the kinematic viscosity) that the two streets may occur in phase or in antiphase. The vortex centres and saddle points of two in-phase streets are antisymmetrical about the flow centreline, but symmetrical for the antiphase case. The in-phase streets eventually merged downstream to form a single street, while the in-antiphase streets remained distinct farther downstream.

Most of the information obtained on the turbulent two-cylinder wake has been based on flow visualization data at a low Re, thus providing only a qualitative description of the flow. Based on ensemble-averaged LDA measurements, Kolář, Lin & Rodi (1997) studied the turbulent near wake of two side-by-side square cylinders for $T/d = 3.0$ and $Re = 23\,100$. They found that the circulation of inner vortices, i.e. those shed on the side towards the flow centreline, decreased faster than that of outer vortices, which were shed on the free-stream side. Their study, however, did not cover the regime of $T/d < 2.0$. Sumner *et al.* (1999) investigated the wake of two and three side-by-side circular cylinders in the range of $T/d = 1$–6 for $Re = 500$–3000. Their flow visualization revealed some interesting details of vortex shedding and the gap flow between cylinders for a relatively high Re. Using a combination of an X-wire and a cold wire, Zhou *et al.* (2000) measured the velocity and temperature fluctuations at $Re = 1800$. They observed that the cross-stream distributions of the Reynolds stresses and heat flux varied significantly as T/d decreased from 3.0 to 1.5, implying a different vortex pattern. Although it is now well-known that the number of vortex streets is different between the two flow regimes, many details of the flow structure, especially the temperature field, remain unknown. Therefore, the first objective of the present work is to study the effect of T/d on the flow structure of the velocity and temperature fields. One may surmise that the momentum and heat transport characteristics of the flow may not be the same as those in a single cylinder wake. The second objective is to understand the manner in which the momentum and heat transport occurs as T/d varies and to compare it with a single-cylinder wake. Following the detection of vortical structures based on the lateral velocity fluctuation, the contribution from the structures is quantified and discussed in the context of the vortex pattern of the velocity and temperature fields. The results point to a significant effect of T/d on the flow structure and transport characteristics. The streamwise evolution of the flow is also discussed in detail.

2. Experimental details

Experiments were carried out in a closed circuit wind tunnel with a square cross-section (0.6 m × 0.6 m) of 2.4 m in length. The wake was generated by two brass cylinders ($d = 12.7$ mm) arranged side-by-side (figure 1). The cylinders were installed horizontally in the mid-plane and spanned the full width of the working section. They were located 20 cm downstream of the exit plane of the contraction. This resulted in a maximum blockage of about 4.2% and an aspect ratio of 47. The transverse spacing between the cylinders was varied from $T/d = 1.5$ to 3.0. Both cylinders were electrically heated. The maximum temperature difference between the heated flow and the ambient fluid, Θ_1, was approximately 1.0 °C. At this level of heating, temperature can be safely treated as a passive scalar at the three measurement stations, $x/d = 10$, 20 and 40, where x is the streamwise coordinate measured from the centre of the cylinder. Measurements were made at a free-stream velocity U_∞ of 7 m s^{-1},

https://doi.org/10.1017/S0022112002007887 Published online by Cambridge University Press

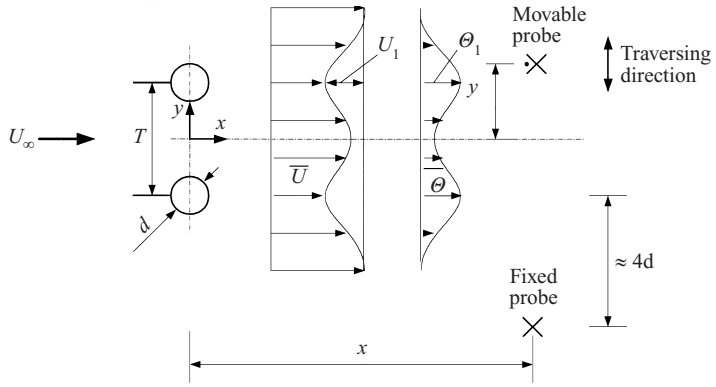


FIGURE 1. Experimental arrangement.

or $Re = 5800$. For the purpose of comparison, the same measurements were also conducted in a single cylinder wake ($T/d = \infty$). In the free stream, the longitudinal turbulence intensity was measured to be approximately 0.4%.

A three-wire probe (an X-wire plus a cold wire, the latter placed about 1 mm upstream of the X-wire crossing point and orthogonal to the X-wire plane) was used to measure the velocity fluctuations, u and v, in the streamwise and lateral directions, respectively, and the temperature fluctuation, θ. The three-wire probe was traversed at an increment of 3 mm across the flow. One X-wire, fixed at $4d$ below the centre of the lower cylinder (figure 1), was used in conjunction with the three-wire probe in order to provide a phase reference for the signals from the three-wire probe. The hot wires were etched from a 5 μm diameter Wollaston (Pt–10% Rh) wire to a length of about 1 mm. For the cold wire, a 1.27 μm diameter Wollaston (Pt–10% Rh) wire was etched to a length of about 1.2 mm and a temperature coefficient of $1.69 \times 10^{-3}\,^{\circ}\mathrm{C}^{-1}$ (Browne & Antonia 1986) was used. Constant-temperature and constant-current circuits were used for the operation of the hot wires and the cold wire, respectively. An overheat ratio of 1.8 was applied for the X-wire, while a current of 0.1 mA was used for the cold wire. The sensitivity of the cold wire to velocity fluctuations was negligible since the length-to-diameter ratio was about 1000. Such a ratio is sufficiently large to allow the neglect of any low-wavenumber attenuation of the temperature variance. The frequency response of the wire, as indicated by −3 dB frequency, was estimated to be 2.2 kHz at the wind speed investigated (Antonia, Browne & Chambers 1981). This was sufficient to avoid any high-frequency attenuation of the main quantities of interest to the present study. Signals from the circuits were offset, amplified and then digitized using a 16 channel (12bit) A/D board and a personal computer at a sampling frequency $f_{sampling} = 3.5$ kHz per channel. The duration of each record was about 10 s.

Noting that the gap flow deflection could change over randomly from one side to the other at $T/d = 1.5$, it would not be desirable if data taken at the same x/d include both modes of gap flow deflection. A test was conducted to estimate the time interval for the gap flow to change its deflection from one side to the other. For a sampling duration of five minutes, only one change was recorded for the present Re. This result was consistent with the measurement by Kim & Durbin (1988), who found that the switching interval of the gap flow deflection was in the order of minutes for $Re = 3.5 \times 10^3$, a few orders longer than the vortex shedding frequency f_s.

https://doi.org/10.1017/S0022112002007887 Published online by Cambridge University Press

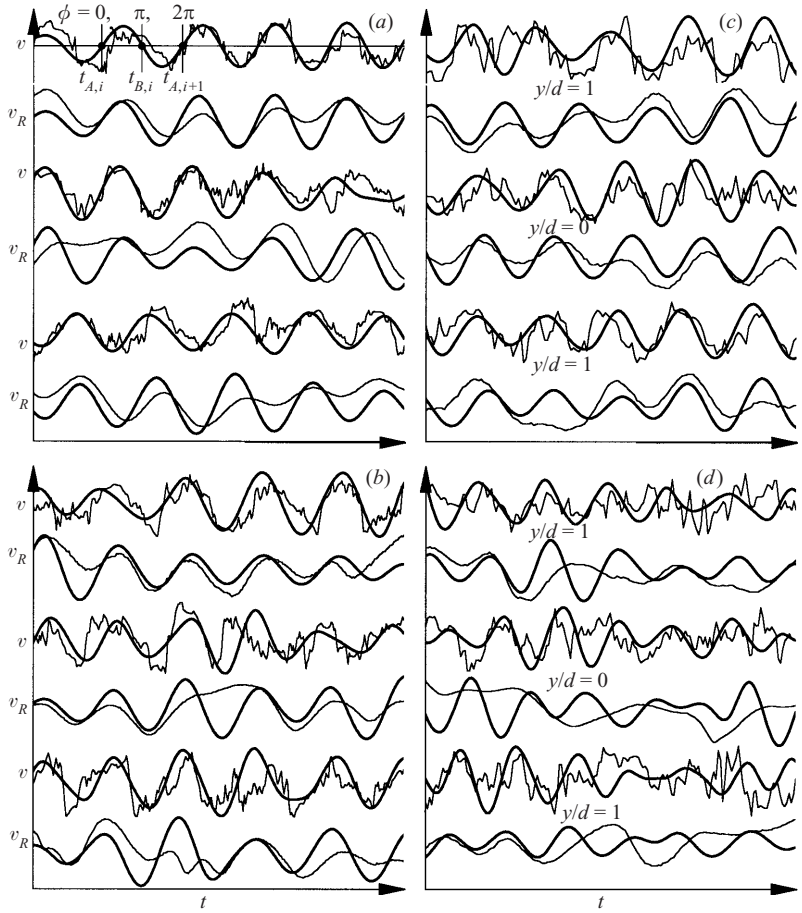


FIGURE 2. Signal v from the movable probe and v_R from the fixed probe. The thicker line represents the filtered signal v_f. (*a*) $T/d = 1.5$, $x/d = 10$; (*b*) 1.5, 40; (*c*) 3.0, 10; (*d*) 3.0, 40.

Therefore, it would be unlikely that the present 10 s sampling duration would include both modes of gap flow deflection. However, the change of gap flow deflection could occur for different points at the same x/d. Great care was taken to avoid collecting these data during experiments. The cross-flow distributions of the mean velocity (§ 4) and Reynolds stresses (§ 6) at each x/d were quite smooth, suggesting an absence of change in the gap flow deflection.

3. Phase and structural averaging

3.1. *Phase averaging*

Vortices shed from a bluff body are characterized by a marked periodicity. In the near or intermediate wake, a small dispersion is expected in the spanwise spacing, lateral location, strength and shape of the vortices. The marked periodicity persists even in the presence of a neighbouring cylinder. Figure 2 illustrates at $T/d = 1.5$ and 3.0 the v-signals from the three-wire probe at a few typical lateral locations, along with the simultaneously obtained reference v_R-signals from the fixed X-wire

https://doi.org/10.1017/S0022112002007887 Published online by Cambridge University Press

probe. The signals exhibit a periodicity. Furthermore, a phase relationship between v and v_R is evident. The spectral phase shift (not shown) at f_s between the v- and v_R-signals at $x/d = 10$ is near zero across the wake for $T/d = \infty$ and 1.5, indicating the antisymmetrical spatial arrangement of vortices. Here, f_s is identified with the frequency where the v-spectrum is maximum. In the case of $T/d = 3.0$, this phase shift is zero for $y/d < 0$ but close to $-\pi$ for $y/d > 0$, suggesting the symmetrical spatial arrangement of vortex streets. (A detailed discussion on the flow structure will be given in § 5). The behaviours of this phase shift at $x/d = 20$ and 40 are similar. Therefore, the u-, v- and θ-signals were phase-averaged. The phase-averaging method is similar to that used by Matsumura & Antonia (1993). Briefly, the v-signals from the two probes were both digitally band-pass filtered with the centre frequency set at f_s. The low- and high-pass frequencies were chosen to be the same as f_s, that is, a zero band-pass width was chosen, following Matsumura & Antonia (1993). This choice allowed a better focus on the vortical structures at f_s. It was tested to allow the low- and high-pass frequencies to be slightly higher and lower than f_s. The flow structure thus obtained was essentially unchanged. A fourth order Butterworth filter was used. The phase shift caused by filtering is very small, about 0.5% of the vortex-shedding period, and almost identical for all signals since the shift depends largely on the filtering frequency set at f_s. The filtered signal v_f is given by the thicker line in figure 2. Two phases of particular interest were identified on v_f, namely

$$\text{Phase A}: \quad v_f = 0 \quad \text{and} \quad \frac{\mathrm{d}v_f}{\mathrm{d}t} > 0,$$

$$\text{Phase B}: \quad v_f = 0 \quad \text{and} \quad \frac{\mathrm{d}v_f}{\mathrm{d}t} < 0.$$

The two phases correspond to time $t_{A,i}$ and $t_{B,i}$ (measured from an arbitrary time origin), respectively. The filtered signal from the three-wire probe was used to determine the phase of the θ-, u- and v-signals of the three-wire probe, namely

$$\phi = \pi \frac{t - t_{A,i}}{t_{B,i} - t_{A,i}}, \quad t_{A,i} \leqslant t \leqslant t_{B,i},$$

$$\phi = \pi \frac{t - t_{B,i}}{t_{A,i+1} - t_{B,i}} + \pi, \quad t_{B,i} < t \leqslant t_{A,i+1}.$$

The interval between phases A and B was made equal to $0.5T_s = 0.5/f_s$ by compression or stretching; it was farther divided into 30 equal intervals. Phase averaging was then conducted on the measured signals, not on the filtered signals. The difference between the local phase at each y-location of the three-wire probe and the reference phase of the fixed X-wire probe was used to produce phase-averaged sectional streamlines or contours of coherent or incoherent quantities in the (ϕ, y)-plane.

The phase average of an instantaneous quantity B is given by

$$\langle B \rangle_k = \frac{1}{N} \sum_{i=1}^{N} B_{k,i},$$

where k represents phase. For convenience, the subscript k will be omitted hereinafter. N is about 600 for $T/d = 1.5$ and 1200 for $T/d = \infty$ and 3.0.

The variable B can be viewed as the sum of the time-mean component $\bar{B}$ and the fluctuation component β. The latter can be further decomposed into the coherent

https://doi.org/10.1017/S0022112002007887 Published online by Cambridge University Press

fluctuation $\tilde{\beta} = \langle\beta\rangle$ and a remainder (incoherent fluctuation) β_r:

$$\beta = \tilde{\beta} + \beta_r.$$

Also,

$$\langle\beta\gamma\rangle = \tilde{\beta}\tilde{\gamma} + \langle\beta_r\gamma_r\rangle,$$

where β and γ can each stand for either u or v or θ.

3.2. *Structural average*

Once the coherent components of the u-, v- and θ-fluctuations are extracted, the coherent contributions to the conventional Reynolds stresses, temperature variance and heat fluxes can be given in terms of the structural average. The conditionally averaged structure begins at k_1 samples (corresponding to $\phi = -\pi$) before $\phi = 0$ and ends at k_2 samples (corresponding to $\phi = \pi$) after $\phi = 0$. The structural average, denoted by a double overbar, is defined by

$$\overline{\overline{\tilde{\beta}\tilde{\gamma}}} = \frac{1}{k_1 + k_2 + 1} \sum_{-k_1}^{k_2} \tilde{\beta}\tilde{\gamma}.$$

The structurally averaged quantities provide a description of the transport characteristics of vortical structures.

4. Time-averaged mean velocity and temperature

Figure 3 shows the cross-stream distributions of the time-averaged streamwise velocity $\bar{U}^*$ and temperature $\bar{\Theta}^*$ of the two-cylinder wake, compared with the single cylinder wake. In this paper, a single overbar denotes conventional time averaging. Here and elsewhere, an asterisk denotes normalization by U_∞, Θ_1 and d. This normalization is used for convenience because the velocity and temperature fields of the present flow are not self-preserving. The experimental uncertainty for time-averaged velocity and temperature is estimated to be 2% and 3%, respectively. This is largely caused by velocity calibration or drifting in hot- and cold-wire performance due to a possible slow change in surrounding conditions. The profiles generally appear reasonably symmetrical about the flow centreline $y^* = 0$, except $\bar{\Theta}^*$ at $T/d = 1.5$. The asymmetry of $\bar{\Theta}^*$ is apparently due to an asymmetrical turbulence field (Zhou *et al.* 2000). Both $\bar{U}^*$ and $\bar{\Theta}^*$ display one single peak around $y^* = 0$ for $T/d = \infty$ and 1.5, but a twin peak for $T/d = 3.0$. These results suggest the occurrence of a single vortex street for $T/d = 1.5$ and $T/d = \infty$, and two streets for $T/d = 3.0$.

The maximum velocity defect, temperature excess, mean velocity and temperature half-widths are summarized in table 1. From $x^* = 10$ to 40, the wake growth for $T/d = 1.5$ and 3.0 is slow, relatively to $T/d = \infty$. For example, the half-width L_u of the mean velocity almost doubles from $x/d = 10$ to 40 for $T/d = \infty$, but increases only about 26% and 27% for $T/d = 1.5$ and 3.0, respectively. A similar observation is made for the temperature field. The half-width L_θ of the mean temperature increases from $x^* = 10$ to 40 by about 160% for $T/d = \infty$ but only 25% for $T/d = 1.5$ and 45% for 3.0. Note that, while the velocity fields at $T/d = 1.5$ and 3.0 grow at the same rate, the temperature field at $T/d = 3.0$ appears to be growing faster. It would seem that the occurrence and interaction of two streets at $T/d = 3.0$ may enhance the entrainment of passive scalars.

https://doi.org/10.1017/S0022112002007887 Published online by Cambridge University Press

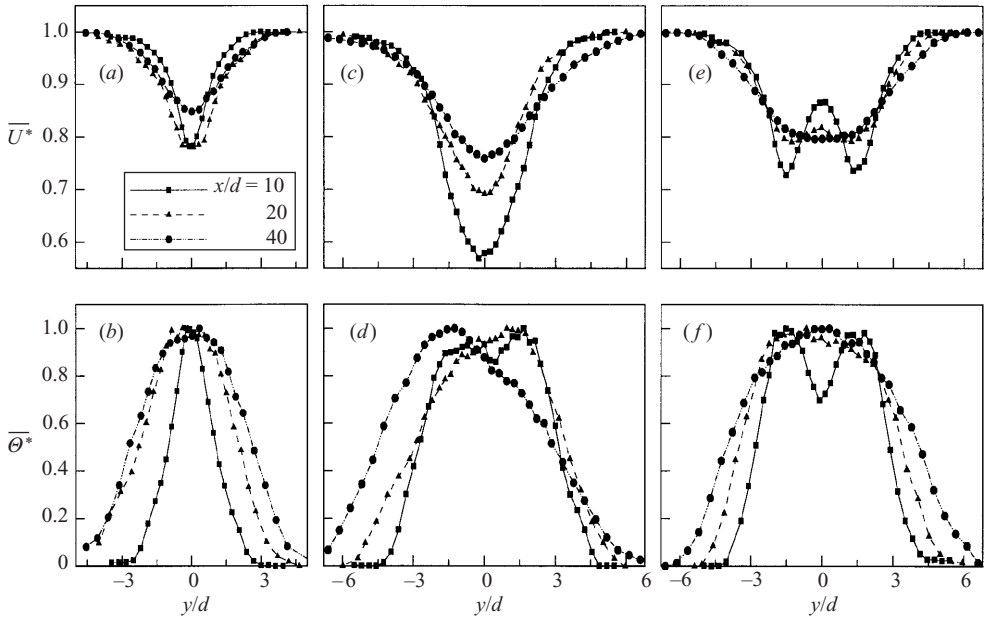


FIGURE 3. Time-averaged streamwise velocity $\bar{U}^*$ and temperature $\bar{\Theta}^*$: (a,b) $T/d = \infty$; (c,d) 1.5; (e,f) 3.0.

T/d	∞			1.5			3.0		
x/d	10	20	40	10	20	40	10	20	40
U_1^*	0.22	0.22	0.16	0.42	0.31	0.24	0.28	0.21	0.20
Θ_1 (°C)	0.73	0.44	0.30	0.89	0.57	0.44	0.69	0.48	0.41
L_u^*	1.58	2.44	2.98	3.84	3.84	4.83	4.79	5.53	6.10
L_θ^*	2.07	4.37	5.36	5.93	6.45	7.46	5.67	6.89	8.19

TABLE 1. Velocity defect, temperature excess and half-width.

5. Phased-averaged velocity and temperature fields

5.1. *Characteristic properties of vortices*

The average convection velocity U_c of vortices is given by the velocity $\bar{U} + \tilde{u}$ at the vortex centre, which is identified with the location of the maximum phase-averaged vorticity $\tilde{\omega}_{max}$. Vorticity is calculated by

$$\tilde{\omega} = \frac{\partial(\bar{V} + \tilde{v})}{\partial x} - \frac{\partial(\bar{U} + \tilde{u})}{\partial y} \approx \frac{\Delta\tilde{v}}{\Delta x} - \frac{\Delta(\bar{U} + \tilde{u})}{\Delta y},$$

where $\Delta x = -U_c \Delta t = -U_c / f_{sampling}$. The estimate of U_c is given in table 2. Upper and Lower in the table stand for the vortices above and below $y^* = 0$, respectively. It will be seen that, at $T/d = 3.0$, two vortex streets occur. Outer in the table denotes the outer vortices, which are shed from the side of a cylinder nearer to the free stream; Inner represents the inner vortices shed from the side of a cylinder close to $y^* = 0$. The result for U_c at $T/d = \infty$ is in good agreement with Zhou & Antonia's (1992) measurement, lending credence to the present estimate. For $T/d = 3.0$, U_c

https://doi.org/10.1017/S0022112002007887 Published online by Cambridge University Press

	T/d		∞			1.5			3.0		
	x/d		10	20	40	10	20	40	10	20	40
y_c^*	Outer	Upper	0.23	0.80	1.29	1.18	1.18	1.89	1.88	2.06	2.44
		Lower				−1.67	−1.10	−1.89	−1.87	−1.97	−2.3
	Inner	Upper							1.24		
		Lower							−1.28		
U_c^*	Outer	Upper	0.86	0.87	0.92	0.77	0.80	0.87	0.83	0.84	0.88
		Lower				0.85	0.81	0.89	0.83	0.84	0.87
	Inner	Upper							0.81		
		Lower							0.81		
$\tilde{\omega}_{max}^*$	Outer	Upper	−1.216	−0.516	−0.151	−0.490	−0.579	−0.184	−0.77	−0.28	−0.10
		Lower	1.267	0.461	0.128	1.025	0.292	0.263	0.85	0.33	0.10
	Inner	Upper							0.63	0.07	
		Lower							−0.72	−0.11	

TABLE 2. Some characteristic properties of vortices.

is practically the same for the upper- and lower-row vortices but the outer vortex appears to have a larger U_c than the inner. The maximum difference in U_c between the inner and outer vortices is about 2.5%. In view of a 2% experimental uncertainty in the estimate of velocity and also experimental uncertainties in locating the vortex centre, this difference may not be statistically significant. There is a considerable difference, about 10% at $x^* = 10$, in U_c between the upper- and lower-row vortices for $T/d = 1.5$, probably because the lower-row vortices are further away from the flow centreline than the upper row. The vortex path, i.e. the most likely lateral distance y_c^* (table 2) of the vortex from the flow centreline, is about 1.67 for the lower vortices and 1.18 for the upper vortices. Note that U_c at $x/d = 20$ is 4.7% smaller than that at $x/d = 10$. The difference is likely due to experimental errors. One error comes from the 2% uncertainty in velocity measurement. Furthermore, since the $\tilde{\omega}^*$ concentration is impaired as x/d increases, an uncertainty in determining y_c^* arises, thus adversely affecting the estimate of U_c. The resulting error in U_c could be up to 3% at $x/d = 20$. This error is even worse for the inner vortices for $T/d = 3.0$. Therefore, the y_c and U_c values of inner vortices are not given in table 2 for $x/d \geqslant 20$. The U_c value of the outer vortex is used to calculate the averaged vortex wavelength, i.e. $U_c T_s = U_c/f_s$.

Power spectra (not shown), calculated from the measured fluctuating velocities without filtering, indicate a single dominant frequency across the wake (this is also true for $T/d = 3.0$). The corresponding Strouhal number $St = f_s d/U_\infty$ is 0.11, about one half of that (0.21) at $T/d = \infty$ or 3.0, in agreement with Zhou *et al.*'s (2000) report. The present measurement fails to detect two different frequencies, as previously reported for $T/d \leqslant 2.0$ by e.g. Ishigai *et al.* (1972). This was initially suspected to be due to a relatively large $x^*(\geqslant 10)$. Therefore, velocity measurements were conducted at $x/d = 2$ using two-component laser Doppler anemometry. Again, one single frequency only (not shown) was detected across the wake. A close examination of the available literature indicates a lack of consistency in the previous reports of vortex frequencies, especially for $1.2 < T/d < 1.5$. Ishigai *et al.* (1972) measured two dominant Strouhal numbers, near 0.1 and 0.3, respectively, for $T/d < 1.25$–1.5. The two Strouhal numbers were detected by Spivack (1946) for $T/d = 1.5$–2.0. Spivac further detected a frequency at 0.2, which could be interpreted as the second harmonic of 0.1. But he failed to detect the frequency 0.3 at $T/d \approx 1.25$. Bearman & Wadcock

https://doi.org/10.1017/S0022112002007887 Published online by Cambridge University Press

(1973) and Kim & Durbin (1988) measured two Strouhal numbers, near 0.1 and 0.3, respectively, for $T/d = 1.5$–2.0, but detected only one dominant frequency, 0.1, for $T/d < 1.5$. Presumably, the generation of gap vortices is essential for the formation of two vortex streets. A very small gap, say $T/d < 1.2$, between the cylinders may prohibit the gap vortices from being generated, and thus the two cylinders behave like a single structure, generating a single vortex street (Sumner *et al.* 1999; Zhou *et al.* 2001). Speculatively, a possible transition occurs for $T/d = 1.2$–1.5 from the regime of a wide and a narrow vortex street to that of a single vortex street. During transition, the gap flow is probably still deflected, as evidenced by different base pressures associated with the two cylinders (Kim & Durbin 1988). But gap vortices may or may not be generated, depending on the initial conditions or experimental set-up. This transition could be responsible for the scattered observations.

A remark is due on the alternating occurrence of the maximum phase-averaged vorticity $|\tilde{\omega}^*_{max}|$ between the upper and the lower row of vortices (table 2). The streamwise meandering motion, if any, of the vortical structures is unlikely to contribute to the observation. Instead, the bi-stability and random changeover of the gap flow deflection, which leads to a significant difference in $|\tilde{\omega}^*_{max}|$ between the two rows of vortices, is probably responsible. While being carefully avoided at the same x/d (§ 2), the changeover may occur for different x/d. This also explains why the $|\tilde{\omega}^*_{max}|$ of the upper vortex at $x/d = 20$ exceeds its counterpart at $x/d = 10$.

5.2. *Vortex patterns*

5.2.1. $T/d = 1.5$

Figures 4 and 5 present the iso-contours of phase-averaged vorticity and the corresponding sectional streamlines. The phase ϕ, ranging from -2π to $+2\pi$, can be interpreted in terms of a longitudinal distance; $\phi = 2\pi$ corresponds to the average vortex wavelength. To avoid any distortion of the physical space, the same scales are used in the ϕ- and y^*-directions in figures 4 and 5 and other figures that follow. A single vortex street is displayed for both $T/d = \infty$ and 1.5, as suggested earlier by the cross-stream distributions of $\bar{U}^*$ and $\bar{\Theta}^*$. The street at $T/d = 1.5$ is however distinctly different from that at $T/d = \infty$. First, the vortices decay slowly, relative to those at $T/d = \infty$. For example, the maximum vorticity at $x^* = 40$ still amounts to about 25% of that at $x/d = 10$ for $T/d = 1.5$, but only 8% for $T/d = \infty$ (12% for $T/d = 3.0$). Secondly, the counter-rotating vortices differ greatly in $|\tilde{\omega}^*_{max}|$ (table 2). This difference diminishes as x/d increases. The $|\tilde{\omega}^*_{max}|$ ratio of the positively signed vortex to that of the negative one is 2.1 at $x^* = 10$ and drops to 1.4 at $x^* = 40$. Thirdly, the flow structure is different, which may be characterized using critical points, i.e. foci, saddle points and nodes (e.g. Zhou & Antonia 1994*a*). The critical points play an important role in the fluid dynamics of a turbulent single cylinder wake, as is well-documented in the literature (e.g. Perry & Chong 1987; Zhou & Antonia 1994*a*). They are expected to play a similar part in a two-cylinder wake, and are therefore not the focus of the present study. Since the vortex centres are presently defined as the location where the maximum concentration of vorticity occurs, the centres will coincide approximately with foci (Zhou & Antonia 1994*a*). The saddle points, identified from the sectional streamlines (figure 5), and vortex centres are marked by '×' and '+' in conditional vorticity contours (figure 4) and some following plots to help interpret data. Evidently, the two cases differ in lateral spacing between saddle points or vortex centres. For example, this spacing for $T/d = 1.5$ is 2.85, 2.28 and 3.8 for $x/d = 10$, 20 and 40, respectively. The corresponding spacing is only 0.46, 1.60 and 2.58 for $T/d = \infty$.

https://doi.org/10.1017/S0022112002007887 Published online by Cambridge University Press

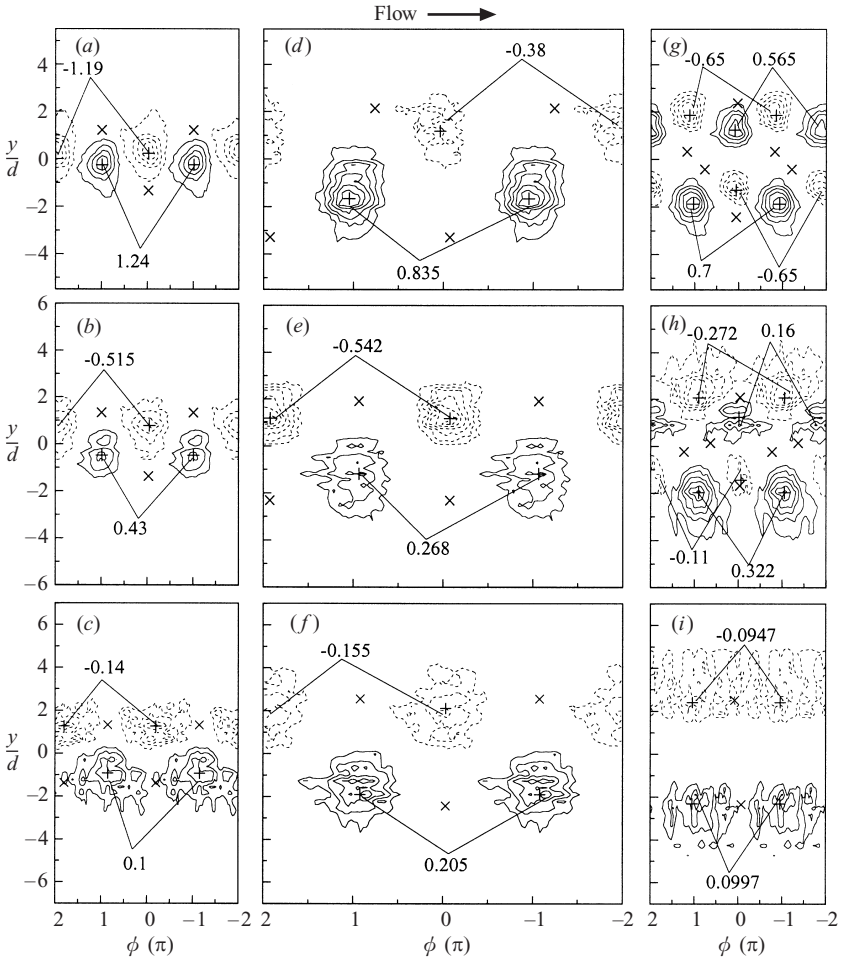


FIGURE 4. Phase-averaged vorticity contours $\tilde{\omega}^*$. (*a–c*) $T/d = \infty$: (*a*) $x/d = 10$, contour interval = 0.27; (*b*) 20, 0.135; (*c*) 40, 0.03. (*d–f*) $T/d = 1.5$: (*d*) 10, 0.135; (*e*) 20, 0.081; (*f*) 40, 0.045. (*g–i*) $T/d = 3.0$: (*g*) 10, 0.135; (*h*) 20, 0.054; (*i*) 40, 0.0243.

Their longitudinal spacing or vortex wavelength is also greater at $T/d = 1.5$ than at $T/d = \infty$.

The phase-averaged sectional streamlines at $x/d = 10$ (figure 5*d*), in particular, those above the flow centreline, appear rather peculiar compared with others. Zhang & Zhou (2001) recently measured the flow (up to $x/d = 10$) behind three side-by-side cylinders ($T/d = 1.5$) using both hot-wire and laser-illuminated flow visualization techniques. They observed a wide wake behind the central cylinder and two narrow wakes on each side of the wide wake. It was found that the vortical structures in the narrow wakes were shed from the cylinder and vanished at $x/d \approx 5$. On the other hand, the vortical structures in the wide wake started to roll up at $x/d \approx 5 (Re > 450)$. They were very weak initially but grew in strength with increasing x/d, resembling those in a screen wake, which were ascribed to the shear layer instability (Zhou & Antonia 1994*b*). This instability differs from that responsible for vortices shed from a cylinder, which decay as x/d increases. The two-cylinder case may bear a resemblance to that of three cylinders. The vortices seen in figures 4 and 5 are formed in the wide

https://doi.org/10.1017/S0022112002007887 Published online by Cambridge University Press

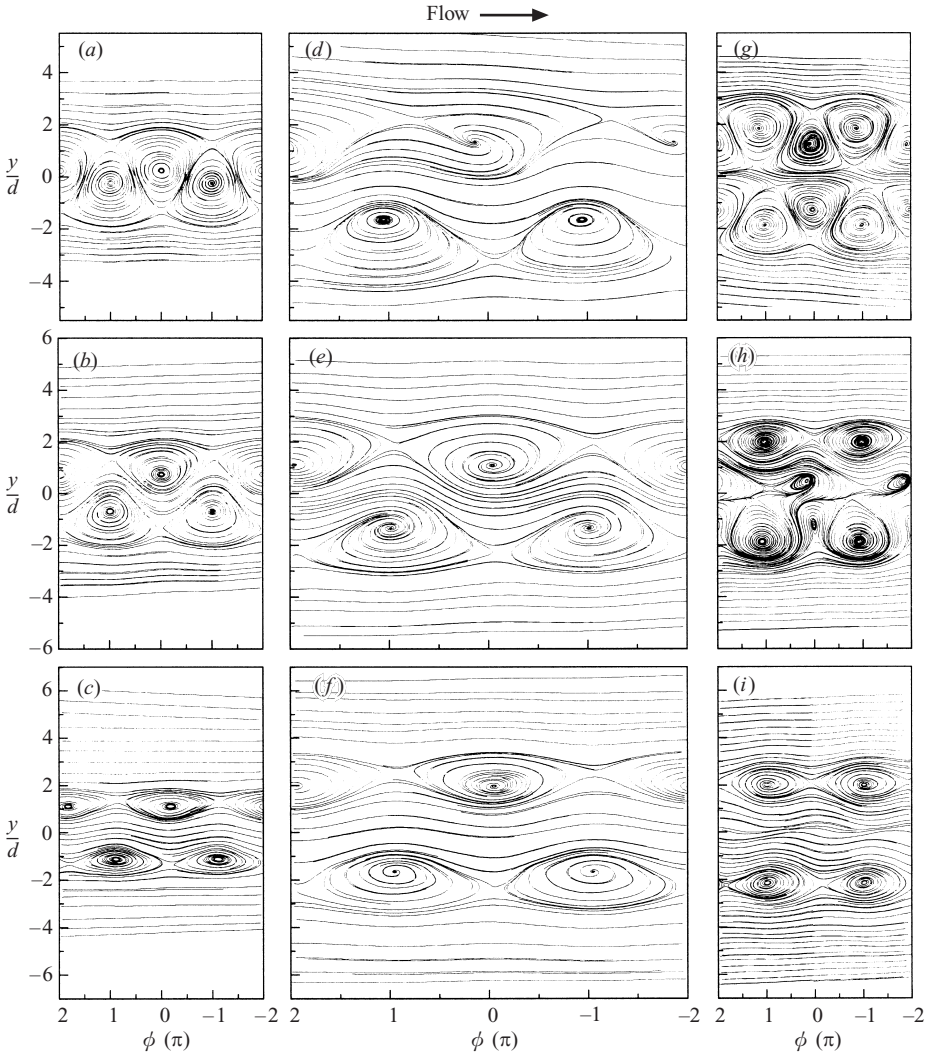


FIGURE 5. Phase-averaged sectional streamlines: (*a*) $T/d = \infty$, $x/d = 10$; (*b*) ∞, 20; (*c*) ∞, 40; (*d*) 1.5, 10; (*e*) 1.5, 20; (*f*) 1.5, 40; (*g*) 3.0, 10; (*h*) 3.0, 20; (*i*) 3.0, 40. The U_c^* values in table 2 are used in the construction of sectional streamlines.

wake, due to the shear layer instability, whereas those in the narrow wake probably disappear before $x/d = 10$. Another scenario of the vortex evolution is the possible coalescence of vortices in the narrow wake with one row of vortices in the wide wake. This was proposed by Williamson (1985) based on the flow visualization behind two side-by-side cylinders at $T/d = 1.5$. Whichever is the case, the vortex regeneration or evolution may not be completed yet at $x/d = 10$. This may contribute to the observation that one row of vortices is relatively weak and also account for the rather peculiar flow pattern at $x/d = 10$. Such a peculiar flow pattern is not seen at $x/d \geqslant 20$ where the vortex regeneration is probably completed.

The gap flow deflection and the formation of wide and narrow wakes behind a row of bluff bodies for $T/d = 1.2$–2.0 have been reported by a number of previous studies (e.g. Ishigai *et al.* 1972; Moretti 1993; Williamson 1985). Some researchers, e.g. Ishigai

https://doi.org/10.1017/S0022112002007887 Published online by Cambridge University Press

et al. and Moretti, attributed the phenomenon to the Coanda effect (Englar 1975). However, Bearman & Wadcock (1973) and Williamson (1985) observed deflected gap flow between two parallel flat plates as well as circular cylinders. This observation suggested that the Coanda effect might not be responsible for the deflection. It is suspected that, since the straight flow in abrupt two-dimensional bluff bodies tends to be unstable, the initial deflection of the gap flow between the cylinders at $T/d = 1.5$ may occur, for example, due to a non-symmetric vortex shedding from the two cylinders. Once the gap flow is deflected, the two streets interact and reach stability in the form of a narrow and a wide wake. The narrow wake is annihilated quickly because of interactions with the wide wake. As a result of the asymmetrical flow condition, the two rows of vortices, generated in the wide wake, are characterized by different vorticity strengths and different distances from $y/d = 0$. The asymmetry of the wake structure should persist at least as long as these vortices survive. Presumably, the interaction between adjacent vortical structures is at least partly responsible for the breakup of vortices. For an isolated cylinder, vortices do not completely vanish until $x/d \approx 40$ or even farther (Hussain & Hayakawa 1987; Zhou & Antonia 1993). For two cylinders spaced at $T/d = 1.5$, the vortices may interact weakly due to relatively large spacing (figures 4 and 5) compared with the $T/d = 3.0$ and ∞ cases, and hence may have a longer lifespan. Indeed, conditional vorticity contours at $x/d = 40$ (figure 4*c*,*f*,*i*) unequivocally point to the longer survival of vortices at $T/d = 1.5$ than the other cases.

5.2.2. $T/d = 3.0$

For relatively large spacing ($T/d > 2$) between two cylinders, two distinct vortex streets of identical dominant frequency occur (e.g. Bearman & Wadcock 1973). For convenience, the U_c associated with the outer vortex is used to construct sectional streamlines in figure 5. That is, identical convection velocities for both inner and outer vortices have been assumed. Tests were conducted to construct sectional streamlines using the convection velocity of the inner vortex; no appreciable change in the flow structure was observed. The two streets are coupled and have a definite phase relationship (Kim & Durbin 1988). This is consistent with our intuition that interactions between two quasi-periodical motions are likely to lead to a coupling between the motions. Indeed, the conditional vorticity contours (figure 4) and sectional streamlines (figure 5) display two vortex streets, symmetrical about $y/d = 0$, up to $x^* = 20$ for $T/d = 3.0$. Previous flow visualization data at low Re suggested that the two streets were predominantly in antiphase immediately behind the cylinders. Ishigai *et al.* (1972) observed a remarkably symmetric vortex formation and shedding for $T/d = 2.5$ and 3.0 Bearman & Wadcock (1973) made a similar observation. Williamson (1985) showed at $Re = 100$–200 that the two streets may occur in phase or in antiphase. The two modes of vortex streets were also evident in Zhou *et al.*'s (2001) flow visualization data ($T/d = 3.0$, $Re = 150$–450). Zhou *et al.*'s simultaneous measurements, using two optical fibre Bragg grating sensors, of vortex-excited vibrations on the two cylinders further pointed to a predominance of the in-antiphase mode vortex shedding for $Re = 800$–$10\,000$. The present observation suggests that the in-antiphase mode streets persist up to at least $x/d = 20$.

One question naturally arises. Can any in-phase mode streets survive or emerge, due to the rearrangement of vortices, downstream say at $x/d = 10$? To address this issue, we attempted to detect two outer rows of vortices and investigate the relative probability of the phase shift between the detections of the two rows. A window average gradient (WAG) method was used for detection. This method is described in

https://doi.org/10.1017/S0022112002007887 Published online by Cambridge University Press

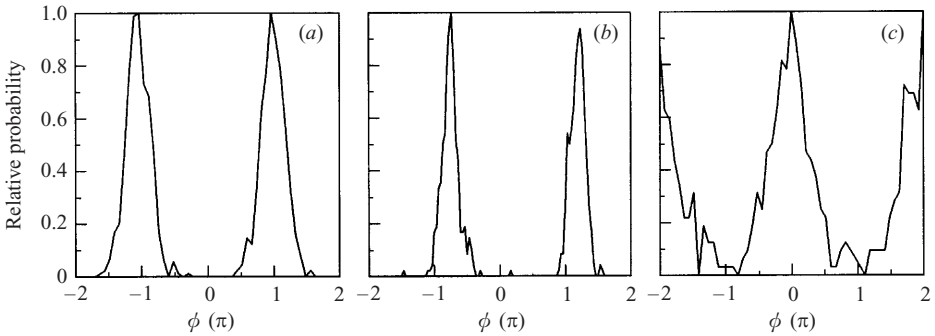


FIGURE 6. Relative probability of phase shift between the WAG detections from the v_R- and the v-signal, which were obtained at $x/d = 10$ and $y/d \approx \pm 4, \pm 4.75$ and ± 5.5 for (*a*) $T/d = \infty$, (*b*) 1.5 and (*c*) 3.0, respectively.

Antonia & Fulachier (1989) and interested readers may refer there for details. Briefly, this scheme examines the u- or v-signal and identifies a change (either an increase or decrease) in average signal level over a specified time interval. The change is associated with the occurrence of vortices. This technique proves to be quite adequate for the detection of vortical structures (e.g. Bisset, Antonia & Britz 1990; Zhou & Antonia 1992 and Zhang, Zhou & Antonia 2000). The lower and upper outer-row vortices (figures 4*g* and 5*g*) were detected based on the v_R-signal ($y/d = -5.5$) and the simultaneously obtained v-signal ($y/d = 5.5$), respectively. A total of about 600 events, which represent about one half of all vortices, were detected. For the purposes of comparison, the WAG technique is also applied to $T/d = \infty$ and 1.5 to detect the two rows of vortices. The relative probability of the phase shift between the two sets of detections is presented in figure 6. The probability has been normalized so that the maximum probability is 1. For $T/d = 3.0$, one prominent peak occurs near $\phi = 0$, indicating predominance by the symmetrical arrangement of vortices. The probability is non-zero near $\phi = \pm\pi$, apparently due to the occurrence of the in-phase vortex streets. If we define $-\frac{1}{2}\pi < \phi < \frac{1}{2}\pi$ as the in-antiphase mode streets and $-\pi < \phi < -\frac{1}{2}\pi$ or $\frac{1}{2}\pi < \phi < \pi$ as the in-phase mode streets, then the former accounts for about 91% and the latter about 9%. The result is internally consistent with both the spectral phase shift at f_s between the v_R- and v-signals and the vortex pattern shown in figures 4(*g*) and 5(*g*). On the other hand, the probability (figure 6*a*, *b*) shows peaks near $\phi = \pm\pi$ and is virtually zero at $\phi = 0$ for $T/d = \infty$ and 1.5, suggesting a predominantly staggered vortex street. The antisymmetrical and symmetrical spatial arrangements of vortices account for 95% and 5%, respectively, for $T/d = 1.5$, and 98% and 2% for $T/d = \infty$. The results conform to figures 4 and 5.

The inner vortices (figure 4*g*, *h*) are weak in terms of $|\tilde{\omega}^*_{max}|$ and small in size compared with the outer vortices. This may be largely due to a faster decay in the inner vortices in the base region. Kolář *et al.* (1997) studied the near-wake of two side-by-side square cylinders ($x^* < 10$, $T/d = 3.0$, where d is the height of the square cylinders) and noted a fast decay in inner vortices. They employed effective turbulent vorticity flux density vector $\boldsymbol{J} = \{J^x, J^y\}$, where

$$J^x = \frac{\partial}{\partial y}\left[\frac{\langle v_r^2\rangle - \langle u_r^2\rangle}{2}\right] + \frac{\partial}{\partial x}\langle u_r v_r\rangle, \tag{1}$$

$$J^y = \frac{\partial}{\partial x}\left[\frac{\langle v_r^2\rangle - \langle u_r^2\rangle}{2}\right] - \frac{\partial}{\partial y}\langle u_r v_r\rangle. \tag{2}$$

https://doi.org/10.1017/S0022112002007887 Published online by Cambridge University Press

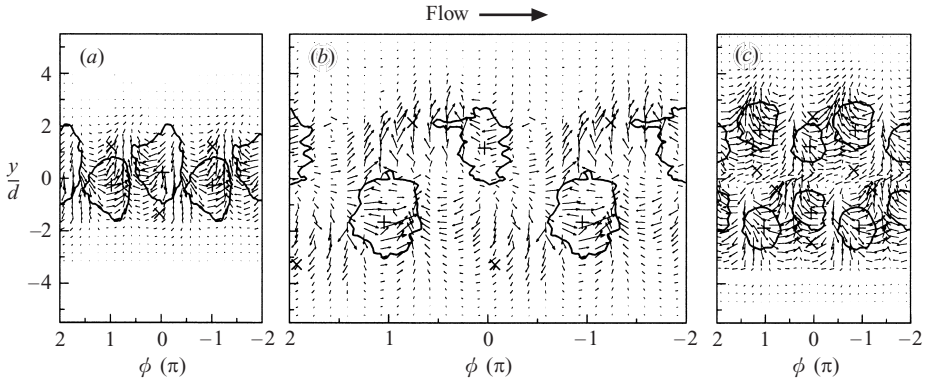


FIGURE 7. Effective vorticity flux density vectors $\tilde{J}^*$ at $x/d = 10$. (*a*) $T/d = \infty$, (*b*) 1.5, (*c*) 3.0. Centres and saddles are denoted by + and ×. The thicker solid line denotes the outermost vorticity contours in figure 4.

As discussed in detail by Hussain (1986) and Kolář *et al.* the vector may indicate the transport of vorticity. Based on phase-averaged $\boldsymbol{J}$, they inferred in the base region that, while an outer vortex interacted primarily with the upstream inner vortex, an inner vortex interacted most vigorously with cross-stream inner vortices, as well as with outer vortices. They suggested that the interaction between the inner vortices shed from the different cylinders was mainly responsible for the fast decay in inner vortices.

The fast decay in inner vortices is also evident in the present data. In fact, the two streets are less stable than the single street at $T/d = \infty$ or 1.5. At $x^* = 10$, the ratio of $|\tilde{\omega}^*_{max}|$ of the inner vortex to that of the outer vortex is about 0.83. It drops to 0.50 at $x/d = 20$. By $x/d = 40$, the vorticity contours (figure 4*i*) show a blank zone in the central region; one street only is identifiable (figure 5*i*).

As shown in figure 6, the vortex streets in both the inphase and antiphase modes exist at x/d beyond 10. The present phase-averaging technique makes no attempt to exclude either mode. Averaging over different modes could result in vorticity cancellation and hence a reduced maximum phase-averaged vorticity. However, this is unlikely to be responsible for the vorticity decay and disappearance of inner vortices in view of the observation that the inphase mode street is only a very small fraction of the antiphase mode street (see figure 6).

Using flow visualization, Williamson (1985) observed in a laminar flow that two in-phase laminar streets formed behind two side-by-side cylinders ($T/d = 4.0$) and then developed into one large-scale single street further downstream. He proposed that like-signed vortices in the two streets paired up and formed binary vortices, which coalesced to form the single street. Such a development was not however observed in Sumner *et al.*'s (1999) PIV data ($Re = 500$–3000). The $\tilde{\omega}^*$ contours (figure 4) and sectional streamlines (figure 5) also do not suggest the coalescence of binary vortices to be a major mechanism behind the present observation in the turbulent wake.

The inner vortices appear squashed, each surrounded by three oppositely signed vortices. One may surmise that the faster decay in vorticity level results from interaction between the oppositely signed vortices. This is indeed supported by effective turbulent vorticity flux density vectors $\boldsymbol{J}$ (figure 7). J^x and J^y were calculated based on (1) and (2):

$$J^x \approx \frac{1}{2}\frac{\Delta\langle v_r^2\rangle - \Delta\langle u_r^2\rangle}{\Delta y} + \frac{\Delta\langle u_r v_r\rangle}{\Delta x}, \tag{3}$$

https://doi.org/10.1017/S0022112002007887 Published online by Cambridge University Press

$$J^y \approx \frac{1}{2}\frac{\Delta\langle v_r^2\rangle - \Delta\langle u_r^2\rangle}{\Delta x} - \frac{\Delta\langle u_r v_r\rangle}{\Delta y}. \tag{4}$$

In the above equations, $\Delta y(= 3\,\text{mm})$ is the spacing between two neighbouring lateral data points. The vector length in figure 7 is proportional to the magnitude of $\boldsymbol{J}$, thus representing the strength of vorticity flux or exchange. The outermost vorticity contour in figure 4, which is the lowest level displaying a clear vortex pattern, is also plotted in figure 7 to indicate approximately the vortex boundary. For $T/d = \infty$, the vorticity flux appears to be moving from one vortex, such as the one at $\phi = 0$, towards the adjacent ones of the opposite sign. The vectors of generally intermediate length cross the vorticity contour both upstream and downstream of the vortices, indicating an exchange in vorticity between counter-rotating vortices. This is not so evident for $T/d = 1.5$, suggesting a relatively weak interaction between oppositely signed vortices, probably because of a large spacing both longitudinally and laterally. The observation is in fact reconcilable with the persistence of vortices for $T/d = 1.5$. The present result at $T/d = 3.0$ is however not quite the same as that inferred by Kolář and his co-workers. At this T/d, relatively long vectors (figure 7*c*) cross the contour of the inner vortex, e.g. at $\phi = 0$ and $y/d < 0$. Part of them meets with those of the opposite direction from the upstream adjacent outer vortex and part of them crosses the flow centreline to interact with others from the cross-stream inner vortex. This observation suggests that the inner vortex exchanges vorticity with both outer vortices shed from the same cylinder and cross-stream inner vortices shed from the different cylinder. However, judging from the vectors crossing the flow centreline (most of which, though not all, appear to originate from the inner vortices), the latter exchange appears comparatively weak, probably due to a relatively large spacing between the inner vortices shed from different cylinders (figure 7*c*). Albeit weak, this exchange would cause additional cancellation in vorticity associated with the inner vortex. On the other hand, the outer vortices appear to interact only with the inner vortices shed from the same cylinder.

Thus a scenario is proposed for the evolution of two streets into a single one. In the base region, the lateral spacing between cross-stream inner vortices is small; the inner vortex interacts vigorously with the cross-stream inner vortices shed from the different cylinder, as well as with the outer vortices shed from the same cylinder. The vorticity exchange between the inner vortices could dominate. In contrast, the outer vortex may largely interact only with the inner vortex shed from the same cylinder. Consequently, the inner vortices decay faster. As x/d increases, the lateral spacing between cross-stream inner vortices becomes larger. On the other hand, the wavelength of quasi-periodic vortices changes little. While the inner vortices still interact with both cross-stream inner vortices and outer vortices, the interaction between the inner and outer vortices shed from the same cylinder now appears to outweigh that between the cross-stream inner vortices shed from different cylinders. The ensuing vorticity cancellation results in the early disappearance of the inner vortices and hence the formation of a single street.

5.3. *The temperature field*

There is a close similarity between the $\bar{\Theta} + \tilde{\theta}$ (figure 8) and $\tilde{\omega}$ contours at $x^* = 10$, suggesting an association of heat with the large-scale vorticity concentration. The similarity disappears at $x^* = 20$ for $T/d = 3.0$ and at $x^* = 40$ for $T/d = \infty$. Evidently, the higher the maximum vorticity level of a vortex, the better the coincidence between the vortex and the higher isotherms. This is illustrated by comparing the $\bar{\Theta} + \tilde{\theta}$ contours (figure 8*d–f*) associated with the two rows of vortices for $T/d = 1.5$. The

https://doi.org/10.1017/S0022112002007887 Published online by Cambridge University Press

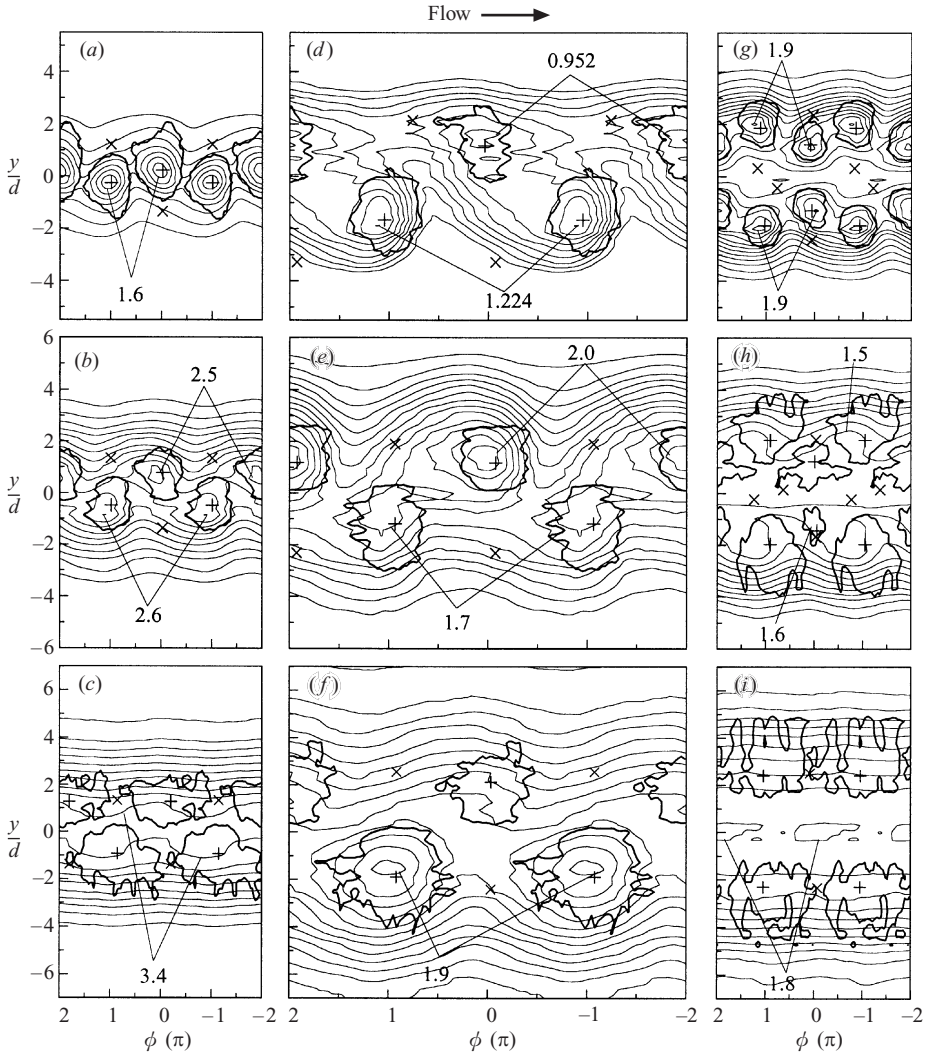


FIGURE 8. Phase-averaged temperature contours $\bar{\Theta}^* + \tilde{\theta}^*$. (*a–c*) $T/d = \infty$: $x/d = 10$, contour interval = 0.2; 20, 0.1; 40, 0.1. (*d–f*) $T/d = 1.5$: 10, 0.136; 20, 0.1; 40, 0.1. (*g–i*) $T/d = 3.0$: 10, 0.1; 20, 0.1; 40, 0.1. The thicker solid line denotes the outermost vorticity contours in figure 4.

row of vortices of larger $|\tilde{\omega}^*_{max}|$ coincides better with higher isotherms than that of smaller $|\tilde{\omega}^*_{max}|$. This observation suggests that a higher concentration of large-scale vorticity, which implies a strong organized motion, retains heat longer. As given in table 2, $|\tilde{\omega}^*_{max}|$ at $x^* = 40$ is 0.263 for $T/d = 1.5$, considerably larger than 0.151 for $T/d = \infty$; it is smallest at all stations for $T/d = 3.0$. This explains the observation that the similarity between the $\bar{\Theta} + \tilde{\theta}$ and $\tilde{\omega}$ contours disappears rather early for $T/d = 3.0$, while higher isotherms still coincide reasonably well with the vortices of relatively large $|\tilde{\omega}^*_{max}|$ (the lower row) at $x^* = 40$ for $T/d = 1.5$. Note that the lower isotherm is drawn in, towards the flow centreline, quite evenly from both sides of the flow for $T/d = \infty$ and 3.0, indicating the entrainment of cold fluid from the free stream to the region between the consecutive vortices. For $T/d = 1.5$, however, the lower isotherm is drawn in largely from one side only by the vortex of relatively large

https://doi.org/10.1017/S0022112002007887 Published online by Cambridge University Press

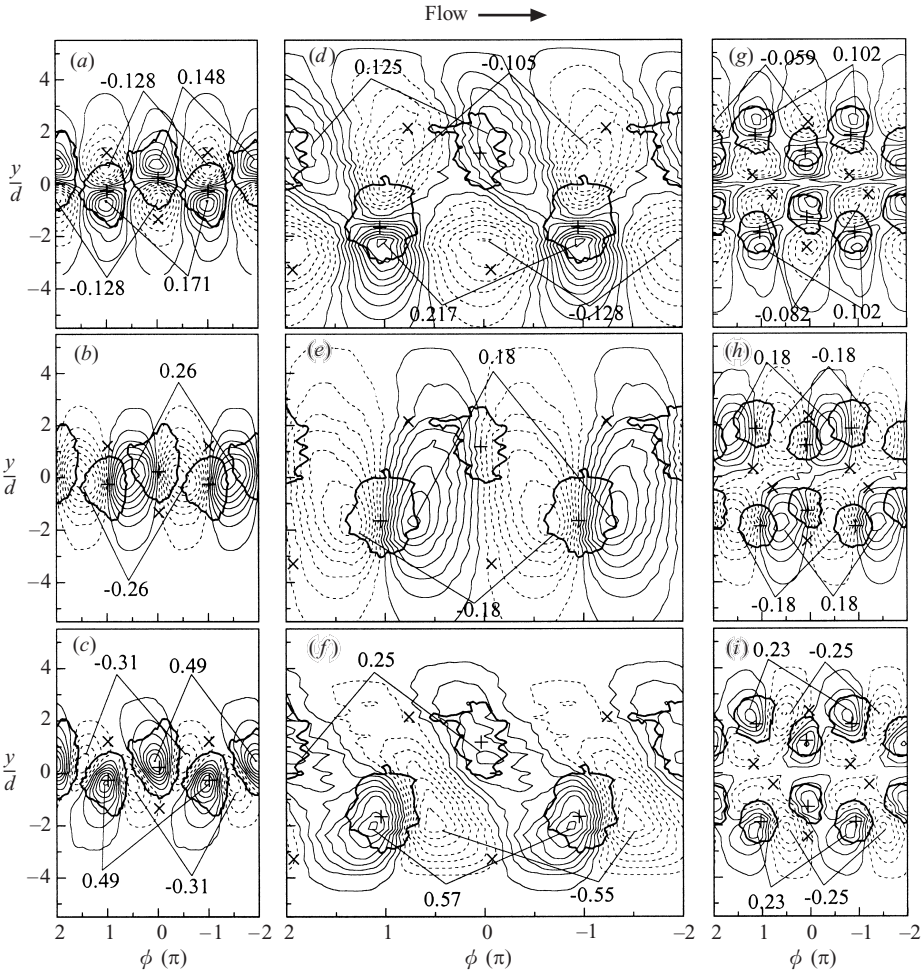


FIGURE 9. Phase-averaged velocity and temperature fluctuations at $x/d = 10$. $\tilde{u}^*$: (*a*) $T/d = \infty$, contour interval = 0.023; (*d*) 1.5, 0.023; (*g*) 3.0, 0.023. $\tilde{v}^*$: (*b*) $T/d = \infty$, contour interval = 0.04; (*e*) 1.5, 0.04; (*h*) 3.0: 10, 0.04. $\tilde{\theta}^*$: (*c*) $T/d = \infty$, contour interval = 0.08; (*f*) 1.5, 0.08; (*i*) 3.0, 0.06. The thicker solid line denotes the outermost vorticity contours in figure 4.

$|\tilde{\omega}^*_{max}|$, for example, from the lower side at $x^* = 10$ (figure 8*d*) and from the upper side at $x^* = 20$ (figure 8*e*).

5.4. *The velocity and temperature fluctuations*

The phase-averaged velocity and temperature fluctuations $\tilde{u}^*$, $\tilde{v}^*$ and $\tilde{\theta}^*$ at $x^* = 10$ are given in figure 9. While the $\tilde{v}^*$ contours display antisymmetry about $\phi = 0$, the $\tilde{u}^*$ contours show approximate up–down antisymmetry about the vortex centre for $T/d = \infty$ and 3, consistent with the interpretation that U_c is close to local $\bar{U}$. For $T/d = 1.5$, however, the up–down antisymmetry of the $\tilde{u}^*$ contours is absent for the upper row of relatively weak vortices. This observation corroborates our earlier suggestion that the formation of vortical structures, originating from the shear layer instability in the wide wake, may not be completed at $x^* = 10$. Consequently, the vortical motion is weak. On the other hand, the $\tilde{u}^*$ contours display the up–down antisymmetry about the centre of the lower row vortex at $x/d = 10$, implying the

https://doi.org/10.1017/S0022112002007887 Published online by Cambridge University Press

completion of the vortical structure formation. The most likely position y_c^* of the upper row vortex is 1.18, nearer to the flow centreline than that, -1.67, of the lower row vortex (table 2), suggesting that the upper row vortex could be initially neighboured by the narrow wake. The observation is consistent with the proposition (§ 5.2.1) that the interaction between the narrow and wide wakes could lead to the early disappearance of the narrow wake and meanwhile contribute to the relatively slow formation of the upper row vortex. For $x^* \geqslant 20$, the negative $\tilde{u}$ (not shown) is present for both rows of vortices and the difference in $\tilde{\omega}_{max}$ reduces.

The appearance of the $\tilde{\theta}^*$ contours for $T/d = \infty$ (figure 9*c*) is similar to that reported by Matsumura & Antonia (1993) and need not be discussed further. For the two-cylinder case, the region near the vortex centre coincides with the positive large-$\tilde{\theta}^*$ contours (figure 9*f*, *i*), apparently resulting from the association of heat with vortices. At $T/d = 3.0$, outer vortices are flanked downstream by the negative contours because of the arrival of cold fluid from the free stream. This is not the case for the upper row vortices at $T/d = 1.5$. The positive-$\tilde{\theta}^*$ contours associated with the upper row vortices are connected with those of the lower row. As discussed earlier, the upper row vortex is rather weak in strength and may not contribute significantly to the entrainment of cold fluid from the free stream. Cold fluid is largely brought in by the lower row vortices. Thus, the lower row vortex is flanked downstream by negative contours.

5.5. *Coherent momentum and heat fluxes*

The $\tilde{u}^*\tilde{v}^*$ contours (figure 10*a*, *d*, *g*) display a clover-leaf pattern about the vortex centre for $T/d = \infty$ and 3.0, which is a result of the coherent velocity field associated with the vortical motion in a reference frame translating at U_c. The near antisymmetry about $\phi = 0$ implies a small net contribution to $\overline{uv}$, due to the cancellation of positive and negative $\tilde{u}^*\tilde{v}^*$. The $\tilde{u}^*\tilde{v}^*$ contours exhibit a quite different structure for $T/d = 1.5$. Those associated with the lower row vortex are quite antisymmetric with respect to $\phi = 0$, again implying a small coherent contribution to $\overline{uv}$. The contours of the upper row vortex are highly asymmetrical about $\phi = 0$; the positive contours are barely identifiable, apparently linked to the weak vortical motion (figure 4*d*). The asymmetry is expected to lead to a large coherent contribution to $\overline{uv}$ from the upper row vortex, as confirmed by a pronounced negative $\overline{uv}$ above $y^* = 0$ (§ 6).

The positive $\tilde{u}^*\tilde{\theta}^*$ contours (figure 10*b*, *e*, *h*) are dominant in all cases. This is expected since the positive $\tilde{u}^*$ overwhelms the negative (figure 9*a*, *d*, *g*) and hot fluid ($\tilde{\theta} > 0$) is mostly associated with vortices in the near wake (figure 9*c*, *f*, *i*).

For $T/d = 3.0$ and ∞, the negative-$\tilde{v}^*\tilde{\theta}^*$ contours (figure 10*c*, *i*) dominate for $y^* < 0$ because the positive and negative $\tilde{v}$ are associated with cold ($\tilde{\theta} < 0$) and warm ($\tilde{\theta} > 0$) fluids, respectively. For $y^* > 0$, the positive and negative $\tilde{v}$ are associated with hot and cold fluids, respectively. The positive contours subsequently overwhelm the negative. Note that at $T/d = 3.0$ the positive and negative contours associated with the inner vortices occur in pairs on either side of a vortex and are comparable in magnitude, which is relatively small. Therefore, the net contribution from the inner vortices to $\overline{v\theta}$ is expected to be negligible, as verified in § 6. It may be concluded that, while neither inner nor outer vortices at $T/d = 3.0$ contribute significantly to the momentum transport, the outer vortices may contribute considerably more to the lateral heat transport than the inner vortices. For $T/d = 1.5$, the upper row vortex is weak and the lower one is strong. Thus, the negative contours associated with the lower vortices overwhelm the positive ones associated with the upper ones. As x^* increases, the difference in vorticity strength between the two rows diminishes (figure 4*d*–*f*).

https://doi.org/10.1017/S0022112002007887 Published online by Cambridge University Press

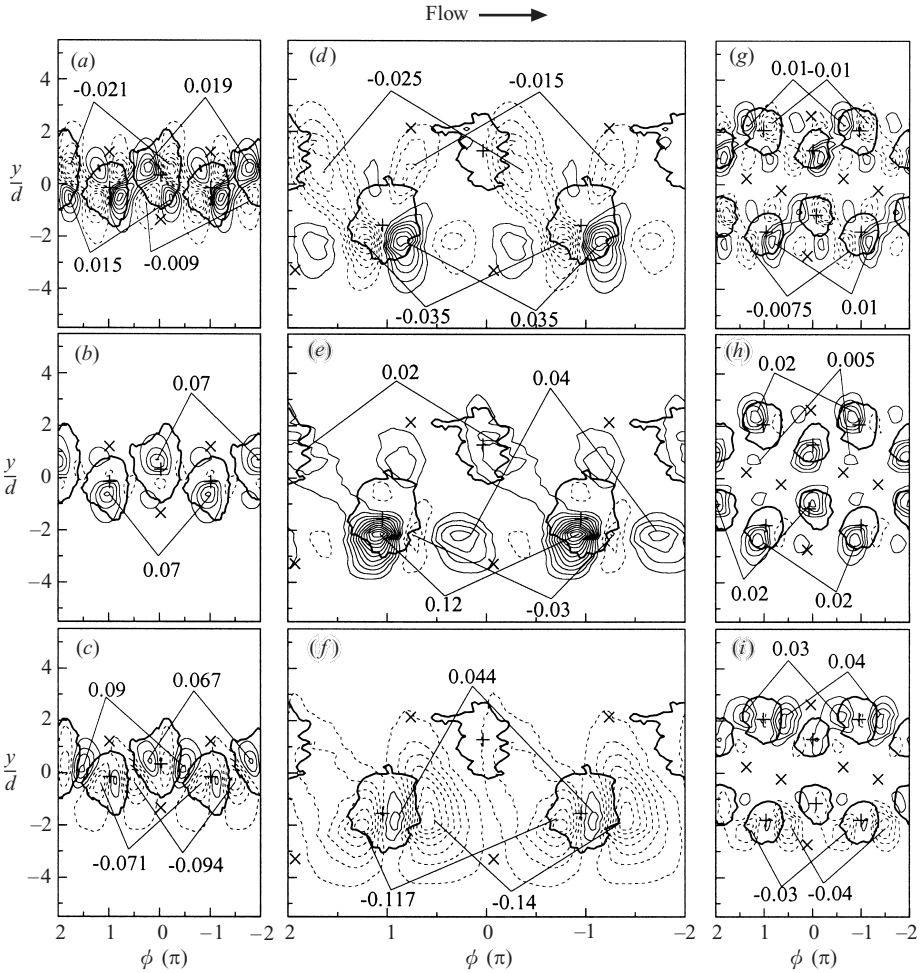


FIGURE 10. Phase-averaged coherent shear stress and heat fluxes ($x/d = 10$). $\tilde{u}^*\tilde{v}^*$: (*a*) $T/d = \infty$, contour interval = 0.004; (*d*) 1.5, 0.005; (*g*) 3.0, 0.0025. $\tilde{u}^*\tilde{\theta}^*$: (*b*) $T/d = \infty$, contour interval = 0.01; (*e*) 1.5, 0.01; (*h*) 3.0, 0.005. $\tilde{v}^*\tilde{\theta}^*$: (*c*) $T/d = \infty$, contour interval = 0.023; (*f*) 1.5, 0.023; (*i*) 3.0, 0.01. The thicker solid line denotes the outermost vorticity contours in figure 4.

5.6. *Incoherent momentum and heat fluxes*

In general, the $\langle u_r v_r \rangle$ contours (figure 11*a*, *d*, *g*) are stretched in the direction of the diverging separatrix and the extremum is near the saddle point where strain is generated because of vortex stretching (e.g. Hussain & Hayakawa 1987). One extremum tends to occur near the vortex centre for $T/d = \infty$ but not for the other cases. Interestingly, although the upper row vortices at $T/d = 1.5$ are weak in strength, the maximum magnitude of the $\langle u_r v_r \rangle$ contours between the consecutive upper row vortices is larger than that between the lower row vortices. Given a certain amount of turbulent energy extracted from the mean flow by the large-scale organized structures, a weak vortical motion (i.e. a small $\tilde{u}\tilde{v}$) is likely to correspond to a strong incoherent motion (i.e. a large $\langle u_r v_r \rangle$). The interpretation is further supported by the observation at $T/d = 3.0$. The inner vortex is relatively weak in strength, its maximum vorticity being about 80% that of the outer vortices (figure 4*g*). This leads to the weak $\tilde{u}\tilde{v}$

https://doi.org/10.1017/S0022112002007887 Published online by Cambridge University Press

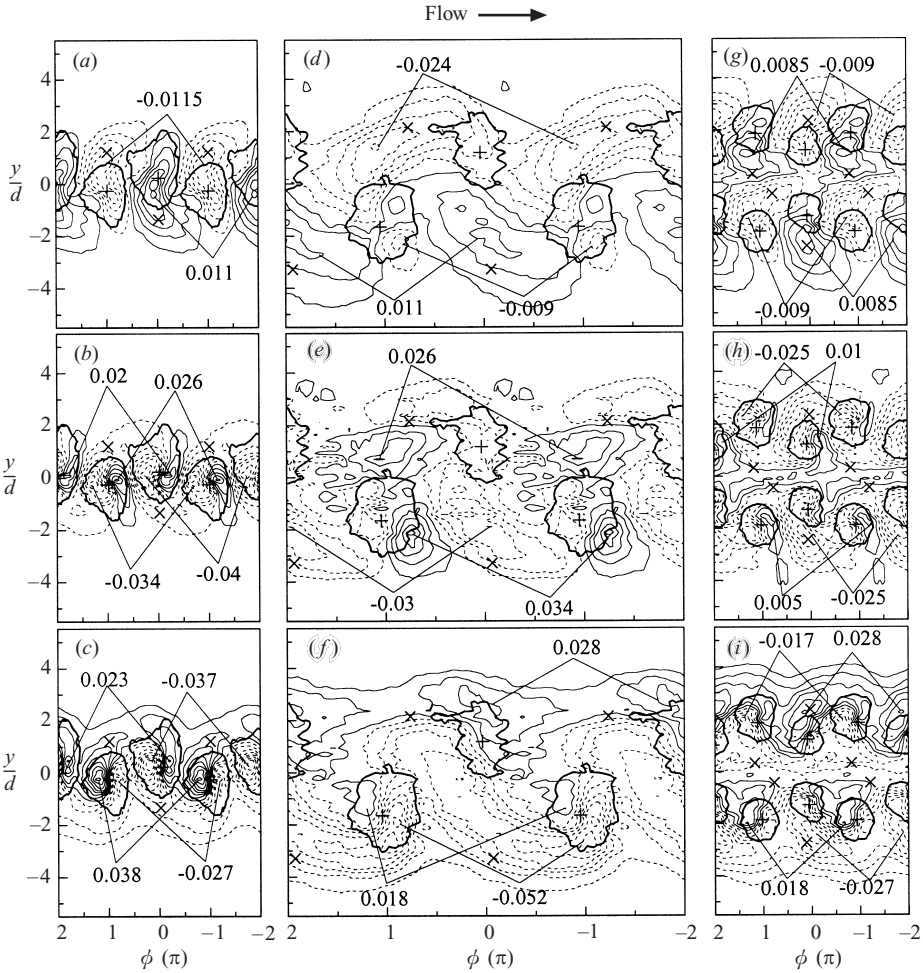


FIGURE 11. Phase-averaged incoherent shear stress and heat fluxes ($x/d = 10$). $\langle u_r^* v_r^* \rangle$: (*a*) $T/d = \infty$, contour interval = 0.0025; (*d*) 1.5, 0.005; (*g*) 3.0, 0.0025. $\langle u_r^* \theta_r^* \rangle$: (*b*) $T/d = \infty$, contour interval = 0.006; (*e*) 1.5, 0.008; (*h*) 3.0, 0.005. $\langle v_r^* \theta_r^* \rangle$: (*c*) $T/d = \infty$, contour interval = 0.005; (*f*) 1.5, 0.01; (*i*) 3.0, 0.005. The thicker solid line denotes the outermost vorticity contours in figure 4.

(figure 10*g*). However, $\langle u_r v_r \rangle$ (figure 11*g*) is quite comparable to that associated with the outer vortex.

The maximum level of the $\langle u_r^* \theta_r^* \rangle$ (figure 11*b*, *e*, *h*) or $\langle v_r^* \theta_r^* \rangle$ (figure 11*c*, *f*, *i*) contours is considerably smaller than that of their coherent counterparts in figure 10. In addition, negative and positive contours associated with vortices occur in pairs, thus cancelling each other at least partially in the calculation of $\overline{u\theta}$ or $\overline{v\theta}$. It may be inferred that the incoherent heat flux is a minor contributor to $\overline{u\theta}$ or $\overline{v\theta}$, as confirmed in § 6 for up to $x^* = 20$, where vortical structures still retain a significant portion of their original strength (figure 4).

6. Coherent contribution to Reynolds stresses and heat fluxes

Time-averaged Reynolds stresses, temperature variance and heat fluxes at $x^* = 10$ and 40 are given in figures 12 and 13. Their experimental uncertainties are estimated

https://doi.org/10.1017/S0022112002007887 Published online by Cambridge University Press

to be 4%, 6% and 5%, respectively. If re-normalized by U_1 instead of U_∞, the single-cylinder data (not shown here) agree both qualitatively and quantitatively with those of Matsumura & Antonia (1993), thus providing a validation of the present measurement. A number of observations can be made. First, the profiles are either quite symmetrical or antisymmetrical about $y^* = 0$ for $T/d = \infty$ and 3.0, but asymmetrical for $T/d = 1.5$. Second, the variances at $T/d = 1.5$ have a larger lateral spread, though only slightly, than those at $T/d = 3.0$, in spite of the fact that the corresponding L_u and L_θ (table 1) are generally smaller. This observation is consistent with a larger scale of vortices at $T/d = 1.5$ (§ 5). Third, the maximum magnitude of the Reynolds stresses and heat fluxes decays appreciably slower at $T/d = 1.5$.

Figure 12 includes the coherent and incoherent contributions to Reynolds stresses, temperature variance and heat fluxes at $x^* = 10$. A few comments can be made:

(i) The coherent contribution to $\overline{u^2}$, $\overline{v^2}$ and $\overline{\theta}^2$ is generally quite significant because of the relatively strong coherent motion in the near wake. vidently, $\overline{\tilde{v}^2}/\overline{v^2}$ is considerably larger than $\overline{\tilde{u}^2}/\overline{u^2}$ and $\overline{\tilde{\theta}^2}/\overline{\theta^2}$, irrespective of T/d. This observation, previously reported by Kiya & Matsumura (1985) and Antonia (1991) for the single-cylinder case, is largely ascribed to the enhancement of $\tilde{v}$ due to the primarily antisymmetrical arrangement of the counter-rotating vortices in a vortex street (figures 4 and 5). Furthermore, the present detection of organized motion is based on the v-signal only and thus $\overline{\tilde{u}^2}$ and $\overline{\tilde{\theta}^2}$ may be underestimated, relative to $\overline{\tilde{v}^2}$.

(ii) At $T/d = 3.0$, $\overline{\tilde{u}^{*2}}$ displays four peaks and $\overline{\tilde{v}^{*2}}$ and $\overline{\tilde{\theta}^{*2}}$ exhibit two peaks, doubling their counterpart for $T/d = 1.5$ and ∞ because of the occurrence of two vortex streets at $T/d = 3.0$ (figures 4 and 5). The coherent contribution to the Reynolds stresses and heat fluxes is generally smaller at $T/d = 3.0$ than that at $T/d = \infty$ or 1.5. This may be attributed to the interaction between the two streets at $T/d = 3.0$, which accelerates the decay of vortices. It is pertinent to comment that $\overline{\tilde{\theta}^{*2}}$ is substantially smaller when $|y^*| < 1.5$ than when $1.5 < |y^*| < 3.0$ (figure 12*o*). The former and latter regions correspond to the occurrence of the inner and outer vortices, respectively. Presumably, the inner and outer vortices, when separated from the cylinder, carry the same amount of heat with them. This observation suggests a faster loss of heat from the inner vortex than the outer one.

(iii) At $T/d = 1.5$, the coherent contribution to $\overline{u^2}$, $\overline{v^2}$, $\overline{\theta^2}$, $\overline{u\theta}$ and $\overline{v\theta}$ is considerably smaller for $y^* > 0$ than for $y^* < 0$. This is reversed for $\overline{uv}$. The observation is in conformity with the observation (§ 5) that the upper row vortices are considerably weaker than the lower ones.

(iv) The coherent contribution to $\overline{u\theta}$ and $\overline{v\theta}$ is generally larger than that to $\overline{uv}$. The positive and negative $\tilde{u}\tilde{v}$ contours (figure 10*a*, *d*, *g*) are longitudinally antisymmetrical about the vortex centre, thus cancelling each other out in the calculation of $\overline{uv}$, which mostly resides in the saddle region (Zhou & Antonia 1995). On the other hand, the $\tilde{u}\tilde{\theta}$ contours (figure 10*b*, *e*, *h*) are predominantly positive and the $\tilde{v}\tilde{\theta}$ contours (figure 10*c*, *f*, *i*) are either positive or negative. The ensuing cancellation is minimal. In addition, due to the close association between heat and vortical structures in the near wake, the coherent contribution accounts for most of $\overline{u\theta}$ and $\overline{v\theta}$. It may be inferred that the vortical structures transport heat more efficiently than momentum, as observed by Matsumura & Antonia (1993) for the single-cylinder case. One exception is the coherent contribution to $\overline{u\theta}$ at $T/d = 3.0$; $\overline{\tilde{u}^*\tilde{\theta}^*}$ (figure 12*q*) is of opposite sign to that of $\overline{u\theta}$, except near the centreline of the flow. For $T/d = 1.5$ and ∞,

https://doi.org/10.1017/S0022112002007887 Published online by Cambridge University Press

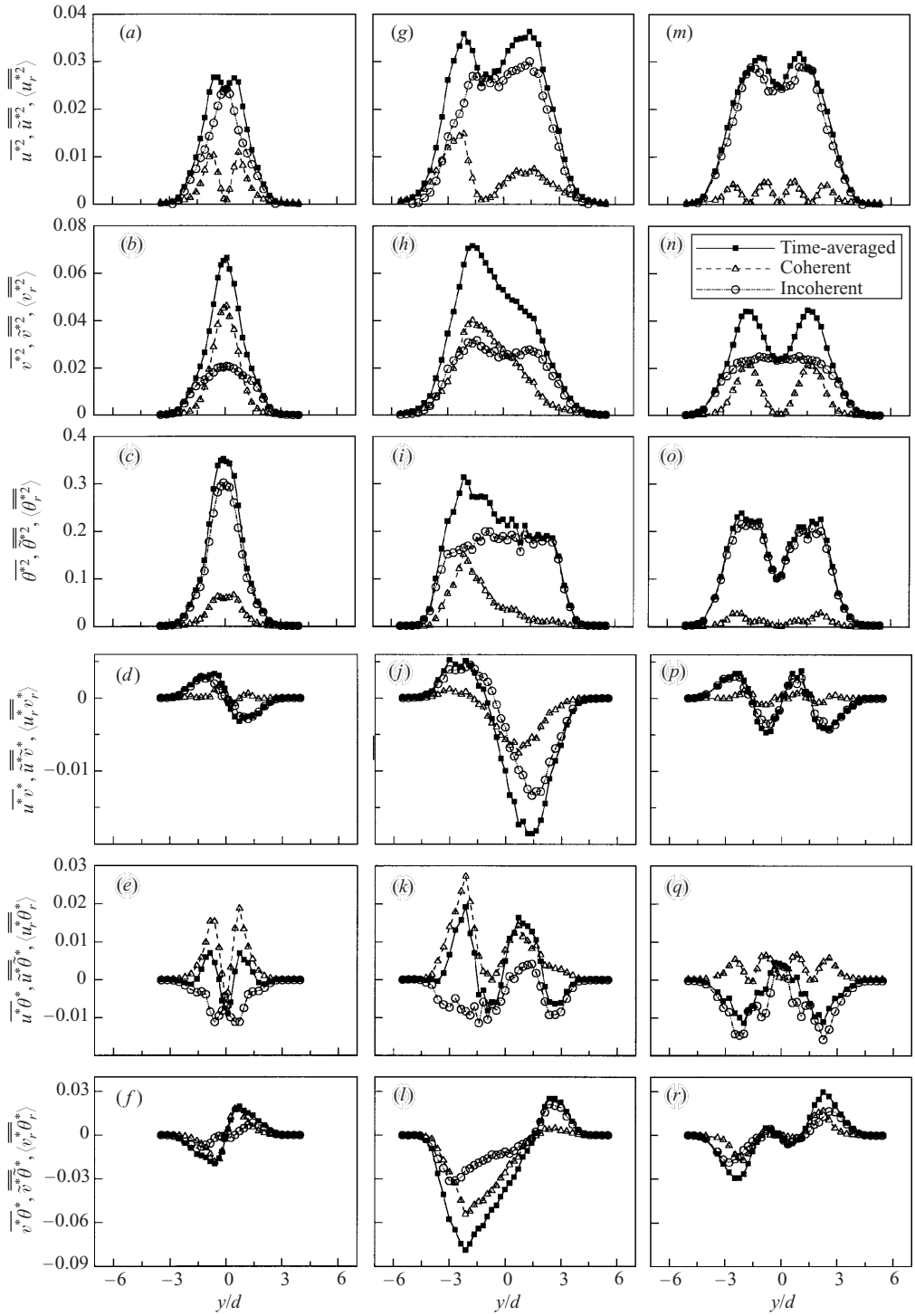


FIGURE 12. Coherent and incoherent contributions to time-averaged Reynolds stresses, temperature variance and heat fluxes at $x/d = 10$: (*a–f*) $T/d = \infty$; (*g–l*) 1.5; (*m–r*) 3.0.

https://doi.org/10.1017/S0022112002007887 Published online by Cambridge University Press

the maximum magnitude of the positive $\tilde{u}^*\tilde{\theta}^*$ (figure 10*b*, *e*), which is associated with vortices, is considerably larger than that of the negative $\langle u_r^*\theta_r^*\rangle$ (figure 11*b*, *e*). But for $T/d = 3.0$, the positive $\tilde{u}^*\tilde{\theta}^*$ (figure 10*h*) and negative $\langle u_r^*\theta_r^*\rangle$ (figure 11*h*) are quite comparable in terms of the maximum magnitude. Further, the latter has a much larger spread both longitudinally and laterally. It is likely that interference between the two vortex streets could greatly hasten the transport of heat out of the vortices. This is supported by the relatively small maximum $\tilde{u}^*\tilde{\theta}^*$ (figure 10*h*) at $T/d = 3.0$ compared with those at $T/d = 1.5$ and ∞ (figure 10*b*, *e*). As a result, $\overline{\langle u_r^*\theta_r^*\rangle}$ exceeds $\overline{\tilde{u}^*\tilde{\theta}^*}$, leading to the observation that $\overline{\tilde{u}^*\tilde{\theta}^*}$ and $\overline{u\theta}$ are opposite in sign. One can expect that the hastened transport of heat from the vortices may also affect the lateral heat transport, but to a lesser degree. The incoherent contribution $\overline{\langle v_r^*\theta_r^*\rangle}$ (figure 12*r*) does account for more of $\overline{v\theta}$ at $T/d = 3.0$ than at $T/d = 1.5$ and ∞ (figure 12*f*, *l*). Note that the $\overline{\tilde{v}^*\tilde{\theta}^*}$ distribution at $T/d = 3.0$ (figure 12*r*) is antisymmetrical about $y^* = 0$, displaying two peaks on either side of $y^* = 0$. The peak near $y^* = 0$, linked to the inner vortex, is substantially smaller than the other, attributed to the outer vortex, corroborating our earlier suggestion that the coherent contribution from the inner vortex is negligibly small.

At $x^* = 40$, there is practically no contribution from the vortical structures to Reynolds stresses and heat fluxes (figure 13), except at $T/d = 1.5$ where the coherent contribution is still appreciable. The streamwise variation of the coherent contribution can be quantified by the dependence of the ratio $\overline{\tilde{\beta}\tilde{\gamma}}/\overline{\beta\gamma}$ on x^*. Since this ratio also varies with y^*, we define an averaged contribution $(\overline{\tilde{\beta}\tilde{\gamma}}/\overline{\beta\gamma})_m$, across the flow, from the vortical structures:

$$(\overline{\tilde{\beta}\tilde{\gamma}}/\overline{\beta\gamma})_m = \int_{-\infty}^{\infty} |\overline{\tilde{\beta}\tilde{\gamma}}|\,\mathrm{d}y^* \Big/ \int_{-\infty}^{\infty} |\overline{\beta\gamma}|\,\mathrm{d}y^*.$$

The values of $(\overline{\tilde{\beta}\tilde{\gamma}}/\overline{\beta\gamma})_m$ are given in table 3. Generally, the coherent contribution is greater to $\overline{v^2}$ than to $\overline{u^2}$. The difference is largest at $T/d = 3.0$. The difference practically vanishes by $x^* = 40$ because of the breaking up or disappearance of the shed vortices. The coherent contribution is smallest to $\overline{\theta^2}$, down to 15–30% at $x^* = 10$. Arguably, heat is initially mostly associated with vortices. The small percentage of the coherent contribution suggests a significant loss of the heat from vortices by $x^* = 10$. The coherent contribution to $\overline{\theta^2}$ drops fastest at $T/d = 3.0$. As x^* increases from 10 to 20, $(\overline{\tilde{\theta}^2}/\overline{\theta^2})_m$ decreases by a factor more than 3 but less than 2 for $T/d = \infty$ or 1.5 (also refer to figure 12*c*, *i*, *o*). The interaction between the two streets may have accelerated the loss of heat. In spite of the substantial heat loss, the coherent contribution to $\overline{u\theta}$ and $\overline{v\theta}$ is greater than to $\overline{uv}$. This reinforces the earlier remark that vortices transport heat more efficiently than they transport momentum, irrespective of the presence of a neighbouring cylinder.

The $(\overline{\tilde{\beta}\tilde{\gamma}}/\overline{\beta\gamma})_m$ value decreases much slower at $T/d = 1.5$ than at $T/d = \infty$ or 3.0. For example, $(\overline{\tilde{v}^2}/\overline{v^2})_m$ at $x^* = 40$ for $T/d = 1.5$ drops only 52%, compared with that at $x^* = 10$, but 91% for $T/d = \infty$ and 98% for $T/d = 3.0$. As noted earlier, the vortices at $T/d = 1.5$ (figures 4 and 5) are characterized by relatively large spacing and hence weak interaction between them, thus surviving longer. In contrast, the interaction between the vortex streets is vigorous at $T/d = 3.0$, resulting in a

https://doi.org/10.1017/S0022112002007887 Published online by Cambridge University Press

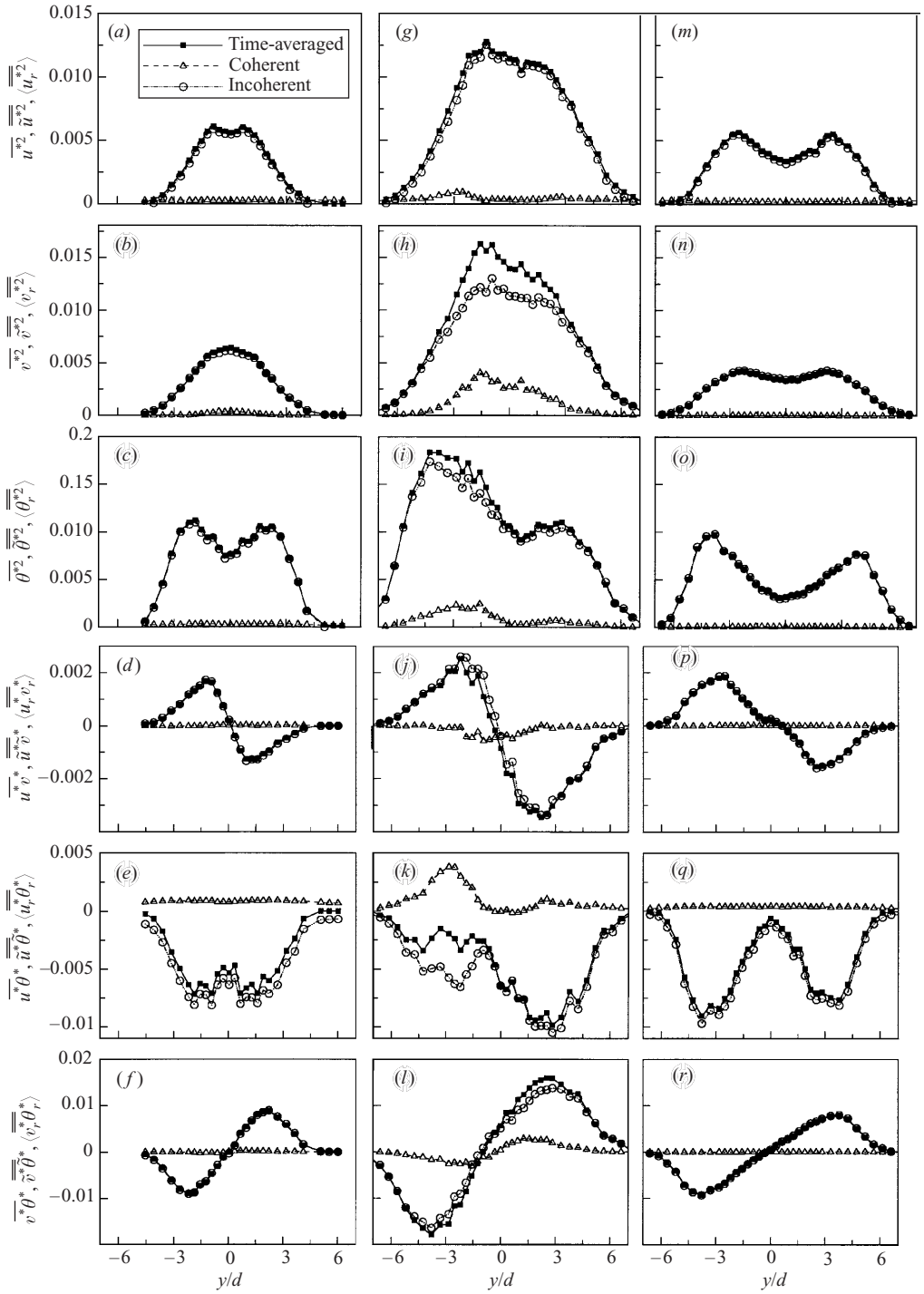


FIGURE 13. Coherent and incoherent contributions to time-averaged Reynolds stresses, temperature variance and heat fluxes at $x/d = 40$: (a–f) $T/d = \infty$, (g–l) 1.5; (m–r) 3.0.

https://doi.org/10.1017/S0022112002007887 Published online by Cambridge University Press

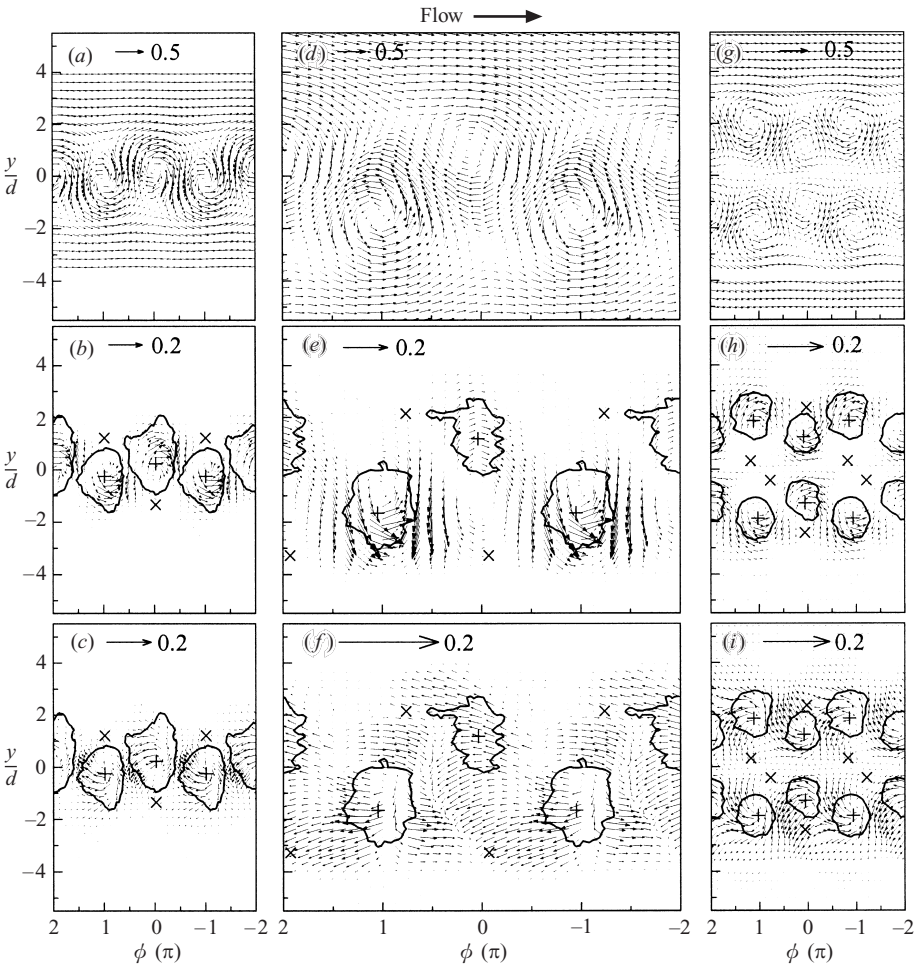


FIGURE 14. Phase-averaged coherent velocity vectors $\tilde{\boldsymbol{V}}^*$ in a reference frame moving at U_c and coherent heat flux vectors $\tilde{\boldsymbol{q}}^*$ and incoherent heat flux vectors $\tilde{\boldsymbol{q}}_r^*$ at $x/d = 10$. $\tilde{\boldsymbol{V}}^*$ (*a*) $T/d = \infty$, (*d*) 1.5, (*g*) 3.0. $\tilde{\boldsymbol{q}}^*$: (*b*) $T/d = \infty$, (*e*) 1.5, (*h*) 3.0. $\tilde{\boldsymbol{q}}_r^*$: (*c*) $T/d = \infty$, (*f*) 1.5, (*i*) 3.0.

shorter vortex lifespan even than that at $T/d = \infty$, and a fast decay in the coherent contribution.

It is worth pointing out that there is no fundamental difference in momentum and scalar transport between the $T/d = \infty$ and $T/d = 3.0$ cases. However, there is a qualitative difference between the $T/d = \infty$ and $T/d = 1.5$ cases. While the transport at $T/d = \infty$ is characterized by symmetry or antisymmetry with respect to $y^* = 0$, the transport at $T/d = 1.5$ behaves very differently from one side of the wake to the other. See $\overline{u^*v^*}$ (figure 12*d*,*j*,*p*) and $\overline{v^*\theta^*}$ (figure 12*f*,*l*,*r*) for example. Zhou *et al.* (2000) measured the turbulent Prandtl number in a three side-by-side cylinder wake. The number was generally about 1 for $T/d = 3.0$, resembling the case of $T/d = \infty$ (Antonia, Zhou & Matsumara 1993), but varied more wildly for $T/d = 1.5$, ranging from near 0 to more than 1. A similar observation was made for the two-cylinder case. It may be concluded that knowledge of flow field changes due to the presence of a neighbouring cylinder is sufficient to predict scalar transport for relatively large T/d, but not for T/d smaller than 2 where gap flow deflection occurs.

https://doi.org/10.1017/S0022112002007887 Published online by Cambridge University Press

T/d	∞			1.5			3.0		
x^*	10	20	40	10	20	40	10	20	40
$(\overline{\tilde{u}^2}/\overline{u^2})_m$ (%)	61.2	14.9	2.4	42.9	27.3	8.0	36.1	4.2	2.9
$(\overline{\tilde{v}^2}/\overline{v^2})_m$ (%)	64.9	33.6	5.9	53.5	40.4	25.4	57.9	23.2	1.3
$(\overline{\tilde{\theta}^2}/\overline{\theta^2})_m$ (%)	19.6	11.4	2.4	31.7	28.3	14.1	14.8	3.9	0.9
$(\overline{\tilde{u}\tilde{v}}/\overline{uv})_m$ (%)	47.7	27.4	4.8	36.9	37.9	17.4	28.1	6.6	2.8
$(\overline{\tilde{u}\tilde{\theta}}/\overline{u\theta})_m$ (%)	147.5	47.3	4.4	83.4	77.2	32.5	76.5	7.2	3.0
$(\overline{\tilde{v}\tilde{\theta}}/\overline{v\theta})_m$ (%)	83.9	36.5	3.4	56.2	39.4	19.2	50.3	15.2	1.0

TABLE 3. Averaged contributions from the coherent motion to Reynolds stresses, heat fluxes and temperature variance.

7. Further discussion

More insight can be gained into the momentum and heat transport characteristics of the flow by examining the coherent heat flux vector $\tilde{\boldsymbol{q}}^* = (\tilde{u}^*\tilde{\theta}^*, \tilde{v}^*\tilde{\theta}^*)$ (figures 14*b*, *e*, *h*) and the incoherent heat flux vector $\tilde{\boldsymbol{q}}_r^* = (\langle u_r^*\theta_r^*\rangle, \langle v_r^*\theta_r^*\rangle)$ (figure 14*e*, *f*, *i*), along with the velocity vector $\tilde{\boldsymbol{V}}^* = (\bar{U}^* + \tilde{u}^* - U_c^*, \tilde{v}^*)$ (figure 14 *a*, *d*, *g*). The velocity vectors are viewed in a reference frame translating at U_c.

At $T/d = \infty$, the coherent heat flux vectors within vortices are generally aligned with the velocity vectors, suggesting that the coherent motion does not contribute to the net transport of heat out of vortices. On the other hand, the incoherent heat flux vectors point upstream, responsible mostly for the net heat transport out of vortices.

The two-cylinder case is not quite the same. When T/d is small, such as 1.5, one staggered vortex street is formed. One row of vortices is substantially weaker in strength than the other. They differ in terms of the maximum vorticity by a factor of about 2 at $x^* = 10$ (table 2). There is also a considerable difference in their sizes (figure 4 *d*). Correspondingly, the cross-stream distributions of Reynolds stresses are asymmetrical (figures 12 and 13). The coherent heat flux vectors associated with the lower row vortex of a strong coherent motion exhibit a behaviour similar to their counterpart at $T/d = \infty$, but those associated with the upper row vortex are directed towards the downstream vortex of the opposite sign. This observation is reasonable. Under the effect of the vortical motion, albeit weak, warm fluid ($\theta > 0$) downstream of the upper row vortex centre moves downward ($v < 0$), resulting in the negative $\tilde{v}\tilde{\theta}$ (figure 10 *f*). Meanwhile, as earlier noted, the negative-$\tilde{u}$ component associated with this vortex is not seen, presumably due to incomplete vortex formation. The warm fluid is therefore associated with the positive $\tilde{u}$, giving rise to the positive $\tilde{u}\tilde{\theta}$, whose contours are stretched towards the cross-stream vortex downstream (figure 10 *e*). The incoherent heat flux vector $\tilde{\boldsymbol{q}}_r$, at $T/d = 1.5$ (figure 14 *f*) is generally directed upstream of the vortex centre, indicating a transfer of heat out of vortices.

A summary sketch is presented in figure 15(*a*) of the vortex pattern and heat transfer characteristics at $T/d = 1.5$. The lower row vortices of a strong coherent motion play a dominant role in the engulfment of fluid from the free stream. Fluid is drawn into the wake largely, though not exclusively, along the downstream side of these vortices from free stream 2. This differs from the single-cylinder case where fluid is engulfed quite evenly from either side of the wake. The coherent contribution to the Reynolds shear stress from the lower row vortices is negligibly small (figure 12*j*) but

https://doi.org/10.1017/S0022112002007887 Published online by Cambridge University Press

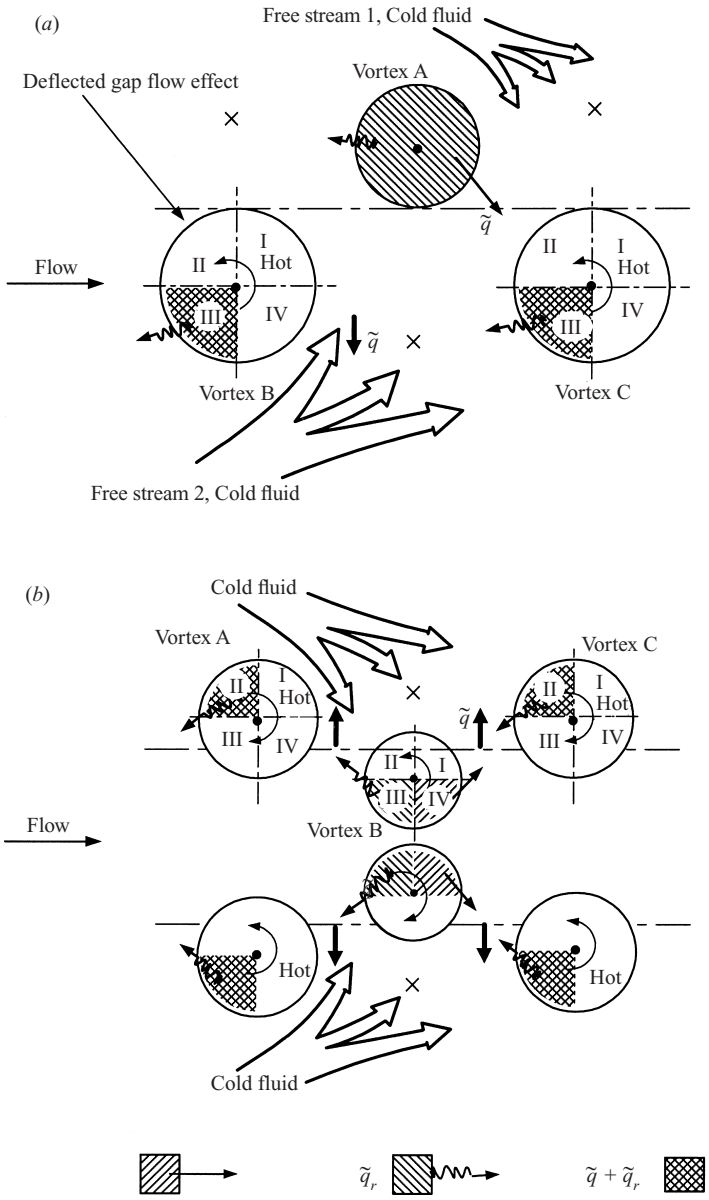


FIGURE 15. Summary sketch of the vortex pattern and transport: (*a*) $T/d = 1.5$; (*b*) 3.0.

accountable for most of the heat fluxes (figure 12*k*, *l*). The lower row vortices do not seem to contribute to any net transport of heat out of the vortices, which is mostly attributed to the incoherent motion. In contrast, the coherent contribution from the upper row vortices could be minor compared to the engulfment of fluid from the free stream and negligibly small compared to the lateral heat flux (figure 12*l*) because of their weak strength. The upper row vortices, however, contribute significantly to the Reynolds shear stress and to the net transport of heat out of vortices.

At $T/d = 3.0$, the vortex pattern is totally different; two predominantly antiphase vortex streets occur. Vortices in each street are again spatially in the staggered arrangement. The outer vortices have a strong coherent motion, relative to the inner

https://doi.org/10.1017/S0022112002007887 Published online by Cambridge University Press

vortices. Since the two streets are arranged symmetrically about the flow centreline, it is sufficient to examine one street only to study the flow.We will focus on the one above the centreline. The coherent heat flux appears to circulate within the outer vortex, implying a small net transport of heat out of the vortex. But $\tilde{\boldsymbol{q}}$ associated with the inner vortices is seen crossing the vorticity contour, pointing partly towards the free stream and partly towards the downstream outer vortex shed from the same cylinder. It has been observed in figure 9(*i*) that the vortical motion coincides with warm fluid ($\theta > 0$), except for the flank of the outer vortices (mostly downstream). Thus, the upward movement (figure 9*h*) of both inner vortices (downstream of the centre) and outer vortices (upstream of the centre) generally corresponds to the positive $\tilde{v}\tilde{\theta}$ (figure 10*i*), the positive $\tilde{u}$ (figure 9*g*) of both inner vortices (below the vortex centre) and outer vortices (above the centre) corresponding to the positive $\tilde{u}\tilde{\theta}$ (figure 10*f*). Therefore, the coherent heat flux (figure 15*b*) is seen flowing largely out of Quadrant IV of the inner vortex B towards the free stream and Quadrant II of the downstream outer vortex C. This is internally consistent with the earlier suggestion that the inner vortices lose heat faster than the outer vortices.

The incoherent flux vector, $\tilde{\boldsymbol{q}}_r$, at $T/d = 3.0$ points upstream within the vortex, as does the $T/d = 1.5$ or ∞ cases. However, upstream of the inner vortex, in particular outside the vorticity contour, $\tilde{\boldsymbol{q}}_r$ is directed towards the free stream. Figure 11(*i*) indicates that above $y^* = 0$, the positive $\langle v_r\theta_r\rangle$ dominates downstream of the outer vortex and upstream of the inner vortex. This is consistent with the arrival of the cold fluid engulfed from the free stream by the upstream outer vortex. Cantwell & Coles (1983) and Hussain & Hayakawa (1987) noted in a single-cylinder case that potential fluid drawn from the free stream by a vortex might be partly assimilated into the vortex on the other side of the wake. The most likely place is Quadrant III of vortex B (figure 15*b*), as suggested by the relatively long length of $\tilde{\boldsymbol{q}}_r$ out of this quadrant (figure 14*i*). Similarly, because the relatively cold fluid is brought from the centreline by the inner vortex, $\tilde{\boldsymbol{q}}_r$ (figure 14*i*) upstream of the outer vortex centre is partly directed towards the centreline, though with a weak strength.

8. Conclusions

The turbulent wake behind two side-by-side circular cylinders has been investigated using a phase-averaging technique. It has been found that the flow structure, heat and momentum transport depend on the cylinder-to-cylinder centre spacing.

At $T/d = 1.5$, a single vortex street is seen throughout the range of $x^* = 10$–40. This vortex street is most stable among the three T/d values investigated. The vortices decay relatively slow. It is noted that the Strouhal number at $T/d = 1.5$, the same across the wake, is about 0.11, half of that for $T/d = \infty$ or 3.0. That is, the longitudinal spacing between vortices is larger at $T/d = 1.5$. Furthermore, the lateral spacing is also considerably greater. The large spacing implies a weak interaction between vortical motions, which is probably responsible for the relatively long lifespan of the vortices and hence the stability of the vortex street. The two rows of vortices behave quite differently. Their convection velocities are not the same at $x^* = 10$ as a result of an asymmetrical spatial arrangement about $y^* = 0$. One row of vortices is significantly weaker in strength than the other. This observation conforms to the asymmetrical distributions of velocity and temperature fluctuations. Speculatively, the vortices occurring at $x/d = 10$ originate from the shear layer instability in the wide wake. The interactions between the narrow and the wide wake are likely to lead to the early vanishing of the narrow wake and, meanwhile, prolong

https://doi.org/10.1017/S0022112002007887 Published online by Cambridge University Press

the formation process of the vortex row that neighbours the narrow wake. On the other hand, the formation of the other row is completed earlier. As a consequence, there is a significant difference in the vortex strengths between the two rows.

As T/d increases to 3.0, the phase-averaged velocity field displays two anti-phase vortex streets of the same vortex frequency. The two streets interact vigorously and are unstable, relative to the cases of $T/d = \infty$ and 1.5. The vortices decay fast, especially the inner ones. By $x^* = 40$, the inner vortex has completely disappears and one street only is discernible. This observation resembles that made by Williamson (1985) in a laminar case, who attributed the development of two streets into one to the coalescence of like-signed vortices. A different interpretation is proposed for the present observation of a turbulent flow. Effective vorticity flux density indicates that, while an outer vortex largely interacts only with adjacent oppositely signed inner vortices, an inner vortex interacts with the cross-stream inner vortices as well as with adjacent outer vortices. As a result, vorticity associated with the inner vortex is annihilated quickly, leading to the early disappearance of inner vortices and the formation of a single street.

The coherent contribution from the vortices to the Reynolds stresses, temperature variance and heat fluxes has been investigated. It has been found that, irrespective of the spacing between cylinders, the vortices transport heat more efficiently than momentum, as reported by Matsumura & Antonia (1993) for the single-cylinder case. However, the spacing between cylinders does have a significant effect on the heat and momentum transport characteristics. Due to the fast decay of vortices at $T/d = 3.0$, the coherent contribution to Reynolds normal stresses and heat fluxes is generally smaller than that for $T/d = 1.5$ or ∞ and drops fast, its level at $x^* = 20$ being comparable with that at $x^* = 40$ of the two other spacing ratios. It is further found that the interaction between the vortex streets at $T/d = 3.0$ hastens, to a great extent, the transport of heat out of the vortices. The inner vortex loses heat even faster than the outer, contributing negligibly to the lateral heat transport. This hastened heat transport leads to the negative coherent contribution to $\overline{u\theta}$. At $T/d = 1.5$, the row of vortices of greater strength makes a large contribution to the Reynolds normal stresses and heat transport, which decays substantially slower because of the relatively stable vortex street, than that at $T/d = 3.0$ or ∞.

The first author wishes to acknowledge support given to him by the Research Grants Council of the Government of the Hong Kong Special Administrative Region through Grant No. PolyU5161/97E.

REFERENCES

Antonia, R. A. 1991 Organization in a turbulent near-wake. *Fluid Dyn. Res.* **7**, 139–149.

Antonia, R. A., Browne, L. W. B. & Chambers, A. J. 1981 Determination of time constants of cold wires. *Rev. Sci. Instrum.* **52**, 1382–1385.

Antonia, R. A. & Fulachier, L. 1989 Topology of a turbulent boundary with and without wall suction. *J. Fluid Mech.* **198**, 429–451.

Antonia, R. A., Zhou, Y. & Matsumara, M. 1993 Spectral characteristics of momentum and heat transfer in the turbulent wake of a circular cylinder. *Expl. Therm. Fluid Sci.* **6**, 371–375.

Bearman, P. W. & Wadcock, A. J. 1973 The interference between a pair of circular cylinders normal to a stream. *J. Fluid Mech.* **61**, 499–511.

Bisset, D. K., Antonia, R. A. & Britz, D. 1990 Structure of large-scale vorticity in a turbulent far wake. *J. Fluid Mech.* **218**, 463–482.

Browne, L. W. B. & Antonia, R. A. 1986 Reynolds shear stress and heat flux measurements in a cylinder wake. *Phys. Fluids* **29**, 709–713.

https://doi.org/10.1017/S0022112002007887 Published online by Cambridge University Press

Cantwell, B. & Coles, D. 1983 An experimental study of entrainment and transport in the turbulent near wake of a circular cylinder. *J. Fluid Mech.* **136**, 321–374.

Englar, R. J. 1975 Circulation control for high-lift and drag generation on STOL aircraft. *J. Aircraft*, **12**, 457–464.

Hussain, A. K. M. F. 1986 Coherent structures and turbulence. *J. Fluid Mech.* **173**, 303–356.

Hussain, A. K. M. F. & Hayakawa, M. 1987 Eduction of large-scale organised structures in a turbulent plane wake. *J. Fluid Mech.* **180**, 193–229.

Ishigai, S., Nishikawa, E., Nishmura, K. & Cho, K. 1972 Experimental study on structure of gas flow in tube banks with tube axes normal to flow. Part 1, Kármán vortex flow around two tubes at various spacings. *Bull. JSME* **15**, 949–956.

Kim, H. J. & Durbin, P. A. 1988 Investigation of the flow between a pair of circular cylinders in the flopping regime. *J. Fluid Mech.* **196**, 431–448.

Kiya, M. & Matsumura, M. 1985 Turbulence structure in the intermediate wake of a circular cylinder. *Bull. JSME* **28**, 2617–2624.

Kolář, V., Lyn, D. A. & Rodi, W. 1997 Ensemble-averaged measurements in the turbulent near wake of two side-by-side square cylinders. *J. Fluid Mech.* **346**, 201–237.

Landweber, L. 1942 Flow about a pair of adjacent, parallel cylinders normal to a stream. D. W. Taylor Model Basin, Department of the Navy, Washington, DC, Report 485.

Matsumura, M. & Antonia, A. 1993 Momentum and heat transport in the turbulent intermediate wake of a circular cylinder. *J. Fluid Mech.* **250**, 651–668.

Moretti, P. 1993 Flow-induced vibration in arrays of cylinders. *Annu. Rev. Fluid Mech.* **25**, 99–114.

Perry, A. E. & Chong, M. S. 1987 A description of eddy motions and flow patterns using critical-point concepts. *Annu. Rev. Fluid Mech.* **19**, 125–155.

Spivack, H. M. 1946 Vortex frequency and flow pattern in the wake of two parallel cylinders at varied spacings normal to an air stream. *J. Aeronaut. Sci.* **13**, 289–297.

Sumner, D., Wong, S. S. T., Price, S. J. & Païdoussis, M. P. 1999 Fluid behaviour of side-by-side circular cylinders in steady cross-flow. *J. Fluids Structures* **13**, 309–338.

Williamson, C. H. K. 1985 Evolution of a single wake behind a pair of bluff bodies. *J. Fluid Mech.* **159**, 1–18.

Zdravkovich, M. M. 1977 Review of flow interference between two circular cylinders in various arrangements. *Trans.* ASME: *J. Fluids Engng* **99**, 618–633.

Zhang, H. J. & Zhou, Y. 2001 Effect of unequal cylinder spacing on vortex streets behind three side-by-side cylinders. *Phys. Fluids* **13**, 3675–3686.

Zhang H. J., Zhou, Y. & Antonia, R. A. 2000 Longitudinal and spanwise structures in a turbulent wake. *Phys. Fluids* **12**, 2954–2964.

Zhou, Y. & Antonia, R. A. 1992 Convection velocity measurements in a cylinder wake. *Exps. Fluids* **13**, 63–70.

Zhou, Y. & Antonia, R. A. 1993 A study of turbulent vortices in the wake of a cylinder. *J. Fluid Mech.* **253**, 643–661.

Zhou, Y. & Antonia, R. A. 1994*a* Critical points in a turbulent near-wake. *J. Fluid Mech.* **275**, 59–81.

Zhou, Y. & Antonia, R. A. 1994*b* Effect of initial conditions on structures in a turbulent near-wake. *AIAA J.* **32**, 1207–1213.

Zhou, Y. & Antonia, R. A. 1995 Memory effects in a turbulent plane wake. *Exps. Fluids* **19**, 112–120.

Zhou, Y., So, R. M. C., Liu, M. H. & Zhang, H. J. 2000 Complex turbulent wakes generated by two and three side-by-side cylinders. *Intl J. Heat Fluid Flow* **12**, 125–133.

Zhou, Y., Wang, Z. J., So, R. M. C., Xu, S. J. & Jin, W. 2001 Free vibrations of two side-by-side cylinders in a cross flow. *J. Fluid Mech.* **443**, 197–229.

https://doi.org/10.1017/S0022112002007887 Published online by Cambridge University Press